

# Phenomenology of the Dark Matter sector in the Two Higgs Doublet Model with Complex Scalar Singlet extension

---

Juhi Dutta,<sup>a</sup> Gudrid Moortgat-Pick<sup>a,b</sup> and Merle Schreiber<sup>a</sup>

<sup>a</sup>*II. Institut für Theoretische Physik*

*Universität Hamburg, Luruper Chaussee 149, 22761 Hamburg, Germany*

<sup>b</sup>*DESY, Notkestraße 85, 22607 Hamburg, Germany*

*E-mail:* [juhi.dutta@desy.de](mailto:juhi.dutta@desy.de), [gudrid.moortgat-pick@desy.de](mailto:gudrid.moortgat-pick@desy.de),  
[merle.schreiber@desy.de](mailto:merle.schreiber@desy.de)

ABSTRACT: Extensions of the Two Higgs Doublet model with a complex scalar singlet (2HDMS) can accommodate all current experimental constraints and are highly motivated candidates for Beyond Standard Model Physics. It can successfully provide a dark matter candidate as well as explain baryogenesis and provides gravitational wave signals. In this work, we focus on the dark matter phenomenology of the 2HDMS with the complex scalar singlet as the dark matter candidate. We study variations of dark matter observables with respect to the model parameters and present representative benchmark points in the light and heavy dark matter mass regions allowed by existing experimental constraints from dark matter, flavour physics and collider searches. We also compare real and complex scalar dark matter in the context of 2HDMS. Further, we discuss the discovery potential of such scenarios at the HL-LHC and at future  $e^+e^-$  colliders.

---

## Contents

|          |   |           |
|----------|---|-----------|
| <b>1</b> | <b>Introduction</b>   | <b>1</b>  |
| <b>2</b> | <b>The Model</b>  | <b>3</b>  |
| <b>3</b> | <b>Complex scalar singlet dark matter phenomenology</b>           | <b>6</b>  |
| <b>4</b> | <b>Experimental constraints</b>                                   | <b>9</b>  |
| <b>5</b> | <b>Allowed parameter regions</b>                                  | <b>10</b> |
| <b>6</b> | <b>Distinguishing between real and complex scalar dark matter</b> | <b>16</b> |
| <b>7</b> | <b>Benchmarks</b>   | <b>17</b> |
| <b>8</b> | <b>Collider Analysis</b>  | <b>20</b> |
|          | 8.1 Prospects at LHC  | 21        |
|          | 8.2 Prospects at $e^+e^-$ colliders                               | 23        |
| <b>9</b> | <b>Summary and Conclusions</b>                                    | <b>29</b> |
|          | <b>References</b>   | <b>32</b> |

---

## 1 Introduction

Dark Matter (DM) remains an unsolved mystery at the interface between particle physics and cosmology. The particulate nature of the dark matter has been under contemplation for several decades and particle physics models providing a possible dark matter candidate are being actively explored at both theoretical and experimental frontiers. A natural candidate for dark matter can be provided by an additional singlet scalar[1, 2] added to the Standard Model (SM) with the SM-like 125 GeV Higgs serving as the portal to the dark sector. However, such minimal Higgs portal dark matter models are constrained stringently from current direct detection data from Xenon-1T[3]. This is a strong motivation to look for non-minimal Higgs portal sectors such as in extended Higgs sectors models. Besides providing dark matter candidates, extended Higgs sectors are also strongly motivated to address some of the still existing open questions in particle physics such as the naturalness problem and baryogenesis. The Two Higgs Doublet model(2HDM)[4] is a minimal extension

of the Standard Model (SM) of particle physics with an extra Higgs doublet. It provides a dark matter candidate only in special cases such as the Inert Doublet model [4]. An extension by a scalar singlet, however, provides a natural DM candidate and presents a portal to the dark matter from both the 125 GeV SM-like Higgs as well as the heavy Higgs sector, enabling additional probes of searching for dark matter at colliders. Singlet extensions can also provide particle physics explanations for baryogenesis and gravitational waves[5]. Real scalar singlet extensions of the 2HDM have been exploited to address the dark matter issue with the heavy CP-even Higgses as portal to DM with discovery potential in the upcoming HL-LHC run [6–8].

Complex scalar extensions to the 2HDM have also been studied in the context of modified Higgs sectors[9, 10], gravitational wave signals and pseudo-Nambu Goldstone dark matter together with a mixed Higgs sector [10, 11]. In this work, we investigate the 2HDMS model where the singlet scalar does not obtain a vacuum expectation value( $vev$ ). This ensures that the Higgs sector is akin to the 2HDM, with five physical Higgs bosons, while the complex scalar singlet is the DM candidate. We study the dark matter phenomenology of this model consistent with all experimental constraints including dark matter, flavour and collider constraints. The presence of the dark matter leads to new decay modes for the Higgs particles opening up into a pair of dark matter particles. We choose representative benchmark points to study collider prospects at both the HL-LHC as well as at future  $e^+e^-$  colliders. Such decays would lead to signatures involving missing energy in the final state at colliders. Furthermore, associated production of the heavy Higgs would lead to signatures involving visible SM quarks/leptons and missing energy signals. We also discuss the viability of observing the channel  $2b+\cancel{E}_T$  channel at the  $e^+e^-$  collider at  $\sqrt{s} = 3$  TeV.

The important points of this work include

- discussion of the parameter space allowed by dark matter constraints in 2HDMS ;
- comparison between the real and complex singlet models with regard to observing the differences between the dark matter phenomenology in both cases;
- identification of some representative benchmarks for 2HDMS allowed by all experimental constraints including dark matter, flavour physics and collider constraints from the SM-like Higgs as well as the heavy Higgs sector;
- discussion of the collider analysis of 2HDMS in the upcoming HL-LHC and future  $e^+e^-$  collider.

The paper is organized as follows: we discuss the model followed by the dark matter phenomenology and collider analyses in Sec. 2- 8. We summarise our results in Sec. 9.

## 2 The Model

We consider the CP-conserving Type II Two Higgs Doublet model (2HDM) augmented with a complex scalar singlet (2HDMS)[9] to avoid flavour changing neutral currents (FCNCs) at tree-level. To consider a more general scenario, one may imply soft  $Z_2$  symmetry breaking consistent with FCNCs. It allows for the presence of the mixing term between  $\Phi_1$  and  $\Phi_2$ , i.e.  $m_{12}^2$  while the explicit  $Z_2$  breaking terms involving the couplings  $\lambda_6$  and  $\lambda_7$  are set to zero. The complex scalar singlet and the dark matter candidate  $S$  is stabilised by a  $Z'_2$  symmetry such that  $S$  is odd under  $Z'_2$  while the SM fields are even under the new  $Z'_2$  symmetry. Extensions of the 2HDM with a real scalar singlet as the dark matter candidate have been studied e.g. in [7]. The quantum numbers of the fields under  $Z_2$  and  $Z'_2$  are given in Table 1. The fields  $\Phi_1$  and  $S$  are even under  $Z_2$  while  $\Phi_2$  is odd under  $Z_2$ . On the other hand, as mentioned above,  $\Phi_1$  and  $\Phi_2$  are even under the new symmetry  $Z'_2$  while  $S$  is odd under  $Z'_2$ . The  $Z'_2$  remains unbroken both explicitly and dynamically, i.e. the singlet doesn't obtain a vev. Therefore, the scalar potential  $V$  with a softly broken  $Z_2$ - and a conserved  $Z'_2$ -symmetry is given by:

$$V = V_{2HDM} + V_S$$

where, the softly broken  $Z_2$ -symmetric 2HDM potential is<sup>1</sup>

$$V_{2HDM} = m_{11}^2 \Phi_1^\dagger \Phi_1 + m_{22}^2 \Phi_2^\dagger \Phi_2 + (m_{12}^2 \Phi_1^\dagger \Phi_2 + h.c.) + \frac{\lambda_1}{2} (\Phi_1^\dagger \Phi_1)^2 + \frac{\lambda_2}{2} (\Phi_2^\dagger \Phi_2)^2 + \lambda_3 (\Phi_1^\dagger \Phi_1) (\Phi_2^\dagger \Phi_2) + \lambda_4 (\Phi_1^\dagger \Phi_2) (\Phi_2^\dagger \Phi_1) + [\frac{\lambda_5}{2} (\Phi_1^\dagger \Phi_2)^2 + h.c.]$$

and the  $Z'_2$ -symmetric singlet potential,  $V_S$ , is

$$V_S = m_S^2 S^\dagger S + (\frac{m_S^{\prime 2}}{2} S^2 + h.c.) + (\frac{\lambda_1''}{24} S^4 + h.c.) + (\frac{\lambda_2''}{6} (S^2 S^\dagger S) + h.c.) + \frac{\lambda_3''}{4} (S^\dagger S)^2 + S^\dagger S [\lambda_1' \Phi_1^\dagger \Phi_1 + \lambda_2' \Phi_2^\dagger \Phi_2] + [S^2 (\lambda_4' \Phi_1^\dagger \Phi_1 + \lambda_5' \Phi_2^\dagger \Phi_2) + h.c.].$$

For simplicity, we set  $\lambda_1'' = \lambda_2''$  without loss of generality throughout our study.<sup>2</sup> Therefore, under the full symmetry  $Z_2 \times Z'_2$  (including softly broken  $Z_2$ ), the scalar potential is,

---

<sup>1</sup>The positive sign convention is used for  $m_{12}^2$  as used for Type II 2HDM implementation in SARAH.

<sup>2</sup>This simplifying assumption was required to disentangle RGEs during implementing this model in SARAH.

| Fields   | $Z_2$ | $Z'_2$ |
|----------|-------|--------|
| $\Phi_1$ | +1    | +1     |
| $\Phi_2$ | -1    | +1     |
| $S$      | +1    | -1     |

**Table 1.** The quantum numbers of the Higgs doublets and the singlet under the  $Z_2$ - and  $Z'_2$ -symmetry.

$$\begin{aligned}
V = & m_{11}^2 \Phi_1^\dagger \Phi_1 + m_{22}^2 \Phi_2^\dagger \Phi_2 + (m_{12}^2 \Phi_1^\dagger \Phi_2 + h.c.) + \frac{\lambda_1}{2} (\Phi_1^\dagger \Phi_1)^2 + \frac{\lambda_2}{2} (\Phi_2^\dagger \Phi_2)^2 \\
& + \lambda_3 (\Phi_1^\dagger \Phi_1) (\Phi_2^\dagger \Phi_2) + \lambda_4 (\Phi_1^\dagger \Phi_2) (\Phi_2^\dagger \Phi_1) + [\frac{\lambda_5}{2} (\Phi_1^\dagger \Phi_2)^2 + h.c.] \\
& + m_S^2 S^\dagger S + (\frac{m'_S}{2} S^2 + h.c.) + (\frac{\lambda''_1}{24} S^4 + h.c.) + (\frac{\lambda''_1}{6} (S^2 S^\dagger S) + h.c.) + \frac{\lambda''_3}{4} (S^\dagger S)^2 \\
& + S^\dagger S [\lambda'_1 \Phi_1^\dagger \Phi_1 + \lambda'_2 \Phi_2^\dagger \Phi_2] + [S^2 (\lambda'_4 \Phi_1^\dagger \Phi_1 + \lambda'_5 \Phi_2^\dagger \Phi_2) + h.c.].
\end{aligned} \tag{2.1}$$

In terms of its components, the Higgs doublets and singlet  $S$  are,

$$\begin{aligned}
\Phi_1 &= (h_1^+ \frac{1}{\sqrt{2}} (v_1 + h_1 + ia_1))^T \\
\Phi_2 &= (h_2^+ \frac{1}{\sqrt{2}} (v_2 + h_2 + ia_2))^T \\
S &= \frac{1}{\sqrt{2}} (h_s + ia_s)
\end{aligned}$$

where  $v_1, v_2$  are the vacuum expectation value ( $vev$ )'s obtained by the neutral components of  $\Phi_1, \Phi_2$ , respectively. Note that the singlet scalar does not obtain a  $vev$ , therefore, the minimisation conditions are

$$\begin{aligned}
m_{11}^2 &= -m_{12}^2 \frac{v_2}{v_1} - \lambda_1 v_1^2 - \lambda_{345} v_2^2 \\
m_{12}^2 &= -m_{12}^2 \frac{v_1}{v_2} - \lambda_2 v_2^2 - \lambda_{345} v_1^2
\end{aligned}$$

After electroweak symmetry breaking (EWSB), there are fifteen free parameters in the theory,

$$\lambda_1, \lambda_2, \lambda_3, \lambda_4, \lambda_5, m_{12}^2, \tan \beta, \lambda''_1, \lambda''_3, m_S^2, m_{S'}^2, \lambda'_1, \lambda'_2, \lambda'_3, \lambda'_4.$$

Here,  $\tan \beta = \frac{v_2}{v_1}$  is the ratio of the  $vev$ 's of the up-type and down-type Higgs doublet denoted by  $v_1 (= v \cos \beta)$  and  $v_2 (= v \sin \beta)$  respectively where  $v (= v_1^2 + v_2^2) \simeq 246$  GeV is the electroweak  $vev$ .

| Particle | $h$                         | $H$                        |
|----------|-----------------------------|----------------------------|
| $u$      | $\cos \alpha / \sin \beta$  | $\sin \alpha / \sin \beta$ |
| $d$      | $-\sin \alpha / \sin \beta$ | $\cos \alpha / \cos \beta$ |
| $l$      | $-\sin \alpha / \sin \beta$ | $\cos \alpha / \cos \beta$ |

**Table 2.** The fermion couplings in the Type II 2HDM[4].

### Fermion and Gauge boson sector

For the Type II 2HDM, the up and down type quarks couple to the two different Higgs doublets. The down-type quarks and leptons couple to  $\Phi_1$  while the up-type quarks couple to  $\Phi_2$ . Thus, the Yukawa Lagrangian is[4]<sup>3</sup>,

$$\mathcal{L}_{Yukawa} = y_u^{ij} Q_i \Phi_2 u_j - y_d^{ij} Q_i \Phi_1 d_j - y_l^{ij} L_i \Phi_1 l_j \quad (2.2)$$

where  $i, j = 1, 2, 3$  are the family indices of the fermions and  $y_f$ , ( $f = u, d, l$ ) are the Yukawa coupling matrices for the quarks and leptons. The couplings of the Higgses to the quarks and leptons (normalized to the SM) are summarised in Table 2[4]. For the couplings to the gauge bosons: the  $HVV$  and  $HHVV$  couplings are suppressed by  $\cos(\beta - \alpha)$  as compared to the SM couplings of the Higgs boson while the couplings of the pseudoscalar to two gauge bosons vanish in the CP-conserving case[4].

### Higgs sector

We now discuss the Higgs sector in this model. The additional complex singlet scalar doesnot develop a  $vev$  and therefore does not mix with the Higgses. Therefore, the Higgs sector remains as in 2HDM consisting of two CP-even neutral scalars Higgses  $h, H$ , a pseudoscalar Higgs  $A$  and a pair of charged Higgses  $H^\pm$ . The mass matrices for the charged, scalar and pseudoscalar sector are [4],

$$M_{\pm}^2 = [-m_{12}^2 - (\lambda_4 + \lambda_5)v_1v_2] \begin{pmatrix} \frac{v_2}{v_1} & -1 \\ -1 & \frac{v_1}{v_2} \end{pmatrix} \quad (2.3)$$

$$M_S^2 = \begin{pmatrix} -m_{12}^2 \frac{v_2}{v_1} + \lambda_1 v_1^2 & m_{12}^2 + \lambda_{345} v_1 v_2 \\ m_{12}^2 + \lambda_{345} v_1 v_2 & -m_{12}^2 \frac{v_1}{v_2} + \lambda_2 v_2^2 \end{pmatrix} \quad (2.4)$$

$$M_{PS}^2 = \frac{m_A^2}{v_1^2 + v_2^2} \begin{pmatrix} v_2^2 & -v_1 v_2 \\ -v_1 v_2 & v_1^2 \end{pmatrix} \quad (2.5)$$

where,  $m_A^2 = [-\frac{m_{12}^2}{v_1 v_2} - 2\lambda_5](v_1^2 + v_2^2)$  and  $\lambda_{345} = \lambda_3 + \lambda_4 + \lambda_5$ . The squared mass of the DM candidate,  $m_\chi^2$ , at tree-level, is

$$m_\chi^2 = m_S^2 + \lambda'_1 \frac{v_1^2}{2} + \lambda'_2 \frac{v_2^2}{2} \quad (2.6)$$

---

<sup>3</sup>The sign conventions for the Yukawa couplings are used as in SARAH for Type II 2HDM.

### Relevant couplings

The Higgses couple to the dark matter giving rise to vertices  $h_iSS$ ,  $h_ih_iSS$  where  $i, j = 1, 2$ . Trilinear couplings to the pseudoscalar are absent at the tree-level due to CP-conservation therefore only  $AASS$  vertices are allowed. The trilinear couplings of the DM with the CP-even Higgses (normalized to  $v$ ) relevant for our discussions later in the section are, while the rest are listed in the Appendix 9.

$$\lambda_{hSS} = \frac{2i}{\sqrt{1 + \tan^2 \beta}} (\lambda'_4 \sin \alpha - \lambda'_5 \tan \beta \cos \alpha) \quad (2.7)$$

$$\lambda_{hS^*S} = \frac{i}{\sqrt{1 + \tan^2 \beta}} (\lambda'_1 \sin \alpha - \lambda'_2 \tan \beta \cos \alpha) \quad (2.8)$$

$$\lambda_{hS^*S^*} = \frac{2i}{\sqrt{1 + \tan^2 \beta}} (\lambda'_4 \sin \alpha - \lambda'_5 \tan \beta \cos \alpha) \quad (2.9)$$

$$\lambda_{HSS} = \frac{-2i}{\sqrt{1 + \tan^2 \beta}} (\lambda'_4 \cos \alpha + \lambda'_5 \tan \beta \sin \alpha) \quad (2.10)$$

$$\lambda_{HS^*S} = \frac{-i}{\sqrt{1 + \tan^2 \beta}} (\lambda'_1 \cos \alpha + \lambda'_2 \tan \beta \sin \alpha) \quad (2.11)$$

$$\lambda_{HS^*S^*} = \frac{-2i}{\sqrt{1 + \tan^2 \beta}} (\lambda'_4 \cos \alpha + \lambda'_5 \tan \beta \sin \alpha) \quad (2.12)$$

### 3 Complex scalar singlet dark matter phenomenology

The complex scalar singlet dark matter candidate  $S$  couples to the Higgses via the Higgs portal terms as in the scalar potential (eq. 2). In a CP conserving scenario, no  $SSA$  or  $SS^*A$ ,  $S^*S^*A$  vertices exist at tree-level. The only interaction of the dark matter to the SM particles is via the Higgses which act as a scalar mediator. Therefore, there are no spin dependent interactions for the dark matter candidate and the only stringent constraints arise from the spin independent DM-nucleon direct detection searches.

#### Relic density

For thermal dark matter, where the DM and SM particles are in thermal equilibrium, the processes contributing to the relic density are the annihilation and co-annihilation process of the DM with the SM particles and itself in the thermal plasma. The processes contributing to the relic density computation are summarised in Fig. 1. Since the only interaction of the DM candidate to the SM particles is via the exchange of Higgses (at tree-level), only s-channel Higgs  $h(H)$  mediated channels as in Fig. 2 contribute besides t-channel contributions mediated via  $S(S^*)$  as in Fig. 3. The relic density therefore depends on the singlet portal couplings  $\lambda'_1, \lambda'_2, \lambda'_4, \lambda'_5$  besides the self interactions of the dark matter  $\lambda''_1, \lambda''_3$ .

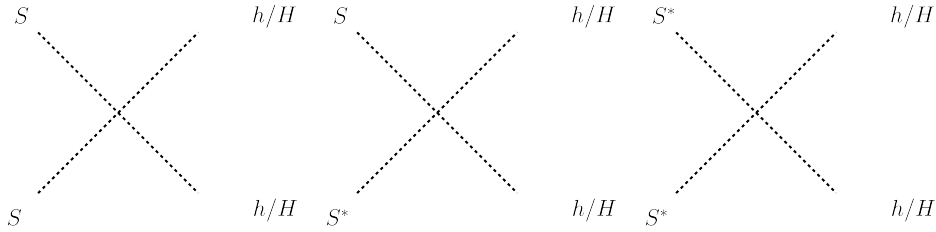


**Figure 1.** The four-point vertices contributing to computation of relic density.

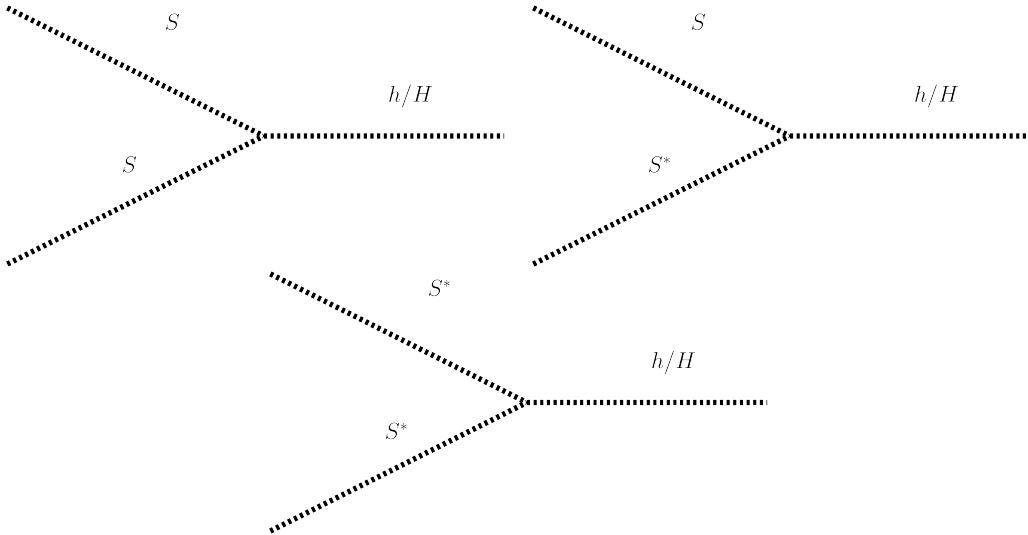


**Figure 2.** The vertices contributing to the  $s$ -channel Higgs mediated processes contributing to computation of relic density. The Higgs decay to all possible final states including fermions, gluons, gauge bosons as well as lighter higgs bosons arising from decay of the heavier CP-even Higgs.

## Direct detection

The interaction of the DM with nucleon are mediated by the  $t$ -channel neutral scalar Higgses at tree-level. The relevant processes are summarised in Fig. 4. The possible vertices involved in these processes are  $\lambda_{h_i SS^*}, \lambda_{h_i SS}$  and  $\lambda_{h_i S^* S^*}$ . The latter two are DM number non-conserving while the former is DM number conserving. For a  $Z_2$  symmetric theory, there is a priori no reason for DM number to be conserved since all of the vertices are allowed by the symmetry arguments. However if a higher theory at ultra-violet (UV) scales lead to a conserved quantum number which one can assign to DM [12, 13], then assuming such a conservation the direct detection cross-sections depend solely on the portal couplings  $\lambda'_1$  and  $\lambda'_2$  since it is the coupling  $\lambda_{h_i SS^*}$  which contributes to the direct detection cross-section. This is solely the consequence under the assumption of an underlying conserved charge corresponding to the dark matter number conservation in presence of the discrete  $Z'_2$  symmetry. For the  $Z_2$  symmetry breaking, the other vertices could give contributions of the

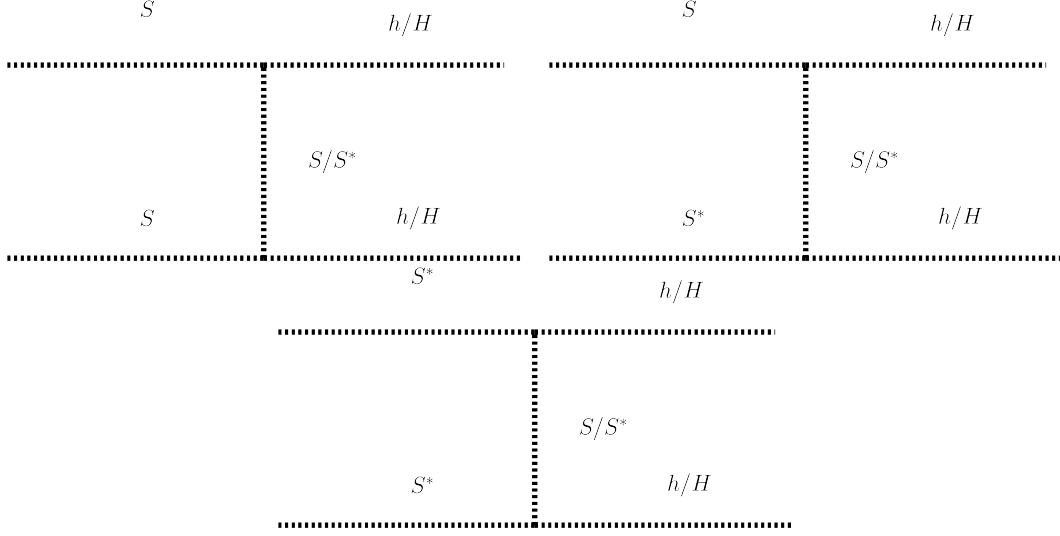


**Figure 3.** The  $t$ -channel mediated processes contributing to computation of relic density.

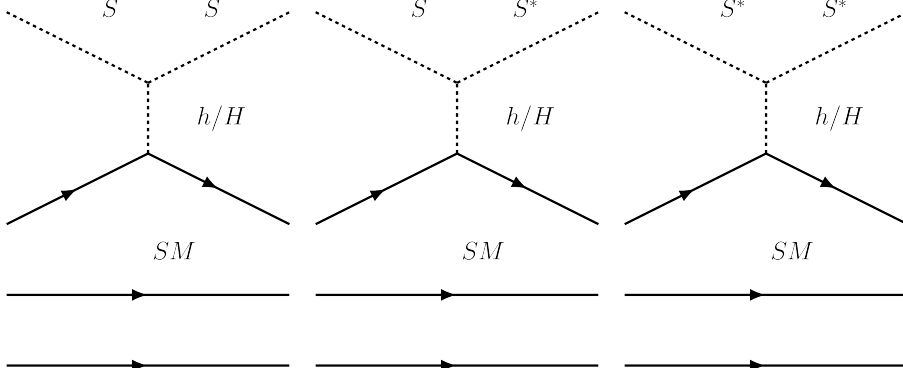


**Figure 4.** Processes contributing to the direct detection of the dark matter candidate  $S$ . Assuming DM number conservation, only the one involving the vertex  $hSS^*$  would contribute while the rest are DM number non-conserving.

same order to the cross-section and hence strongly constrain the current parameter space. We leave this analysis for a future work and proceed with the assumption of a conserved quantum number for the DM. The direct detection cross section rate for the proton and neutron scattering are

$$\sigma_p^{SI} = \frac{4\mu_N^2}{\pi} [f_p Z]^2,$$

$$\sigma_n^{SI} = \frac{4\mu_N^2}{\pi} [f_n (A - Z)]^2,$$

where

$$\mu_N = \frac{m_N m_\chi}{m_N + m_\chi} \quad (3.1)$$

is the reduced mass of the DM-nucleon system where  $N = p, n$  is the nucleon. The couplings of the proton and neutron  $f_p$  and  $f_n$  to the DM are computed from the DM-quark cross section corresponding to Fig. 2. The heavy Higgs mediated processes would be relatively more suppressed because of the propagator suppression due to  $m_H > m_h$ . The DM-quark amplitude  $\mathcal{M}$  is,

$$\mathcal{M} = \sum_i \frac{\lambda_{h_i SS^*} \lambda_{h_i f \bar{f}}}{t - m_{h_i}^2} \quad (3.2)$$

where  $i = 1, 2$  such that  $h_i = h, H$  and  $h_i f \bar{f}$  are the yukawa couplings of the fermions to the Higgses. Assuming DM number conservation and for zero momentum transfer, the propagator reduces to  $\frac{1}{-m_{h_i}^2}$ . The cancellation in the amplitudes for scalar dark matter is affected by the presence of dimension-4 terms U(1) breaking as pointed out in [14] (also [15]) where the terms are loop suppressed arising from the loop corrections. For the  $Z'_2$  symmetry case, such terms are allowed at the tree-level and are not loop-suppressed. Thus, the direct detection cross-section may be affected by the presence of the portal terms at the tree-level and such cancellations between the scalar contributions of the Higgses to the direct detection cross-section may be spoiled.

### Indirect detection

The dark matter self annihilation and via the CP-even Higgses to final state SM particles lead to the indirect detection signatures. Among these signatures, stringent constraints arise from Fermi-LAT [16] on the channels  $b\bar{b}$  and  $\tau\tau$  followed by  $W^+W^-$ . Among new signatures specific to Higgs portal models are di-Higgs channels which are relatively weakly constrained from experiments.

## 4 Experimental constraints

The following experimental constraints are imperative while moving ahead with any BSM theory.

- The lightest CP-even Higgs mass,  $m_h = 125$  GeV within the experimental error [17].
- The invisible decay width of the light Higgs, is constrained by ATLAS and CMS as below,

$$\begin{aligned} BR(h \rightarrow \chi\chi) &\leq 0.11_{-0.03}^{+0.04} \text{ (ATLAS)[18]} \\ &\leq 0.19 \text{ (CMS)[19].} \end{aligned} \quad (4.1)$$

This limit is adhered to by choosing,  $m_{DM} > 62.5$  GeV.

- Flavor physics constraints, namely  $BR(b \rightarrow s\gamma) = (3.55 \pm 0.24 \pm 0.09) \times 10^{-4}$  [20],  $BR(B_s \rightarrow \mu^+\mu^-) = (3.2_{-1.2-0.3}^{+1.4+0.5}) \times 10^{-9}$  [21, 22]. The benchmark points also are within the upper limit of  $\Delta(g-2)_\mu (= 261(63)(48) \times 10^{-11})$  [23].
- The benchmark points also satisfy the electroweak precision test constraints on the STU parameters, where  $S = 0.02 \pm 0.1$ ,  $T = 0.07 \pm 0.12$ ,  $U = 0.00 \pm 0.09$  [24].
- The relic density upper limit from PLANCK data, i.e,  $\Omega h^2 = 0.119$  [25] is adhered to.
- DM-nucleon spin independent cross sections from XENON-1T [3] and indirect detection constraints from Fermi-LAT [16].
- Collider constraints from LEP [26] and Run 2 ATLAS/CMS searches on the heavy Higgs searches [27, 28] and the 125 GeV Higgs signal strength measurements [29].

The Higgs sector of 2HDMS is the same as in the 2HDM (for current status refer to [30, 31]). For the 2HDMS, we compute the DM relic and direct detection constraints using micrOMEGAs [32]. Constraints on the Higgs sector are checked using HiggsBounds and HiggsSignals [33]. B-physics constraints are checked using SPheno-v4.0.4 [34].

## 5 Allowed parameter regions

In this section, we discuss the allowed parameter regions from the dark matter constraints of relic density and spin independent direct detection cross-section. We perform a scan using the parameters summarised in Table 3. The model is implemented using SARAH-v4.14.3 [35] and SPheno-4.0.4 [34] is used for generating the particle mass spectrum and decays, and performing the parameter scans.

### Relic Density

In Fig. 5, we observe that the relic density of the complex scalar dark matter is satisfied at the resonance region corresponding to the lightest CP-even 125 GeV Higgs. One should note however no funnel regions corresponding to heavy higgs annihilation are observed for the parameter values fixed for the scans. However these regions are accessible for large values of the portal couplings (close to the perturbativity limit). This is due to an interplay of the couplings and mass of the heavy higgs while determining the cross-sections during the relic density computation.

In Fig. 1 there is a rapid change observed in the relic density near the  $m_\chi \simeq 75$  GeV where the thermal relic density is achieved. We focus on this region of light

| Parameters                     | BPA                |
|--------------------------------|--------------------|
| $\lambda_1$                    | 0.23               |
| $\lambda_2$                    | 0.25               |
| $\lambda_3$                    | 0.39               |
| $\lambda_4$                    | -0.17              |
| $\lambda_5$                    | 0.001              |
| $m_{12}^2$ (GeV <sup>2</sup> ) | $-1.0 \times 10^5$ |
| $\lambda_1''$                  | 0.1                |
| $\lambda_3''$                  | 0.1                |
| $\lambda_1'$                   | 0.042              |
| $\lambda_2'$                   | 0.042              |
| $\lambda_4'$                   | 0.1                |
| $\lambda_5'$                   | 0.1                |
| $m_S^{2'}$ (GeV <sup>2</sup> ) | $1.13 \times 10^5$ |
| $m_h$ (GeV)                    | 125.1              |
| $m_H$ (GeV)                    | 724.4              |
| $m_A$ (GeV)                    | 724.4              |
| $m_{H^\pm}$ (GeV)              | 728.3              |
| $m_\chi$ (GeV)                 | 338.9              |
| $\tan \beta$                   | 5                  |

**Table 3.** List of parameters kept fixed for the scans for relic density and direct detection cross-section along with the mass of the Higgses and dark matter candidate.

| Parameters | $m_S^2$ (GeV <sup>2</sup> ) | $\tan \beta$ |
|------------|-----------------------------|--------------|
| Values     | 100-400000                  | 5            |

**Table 4.** Range of relevant parameters varied for the scans involving relic density and direct detection cross-section versus dark matter mass,  $m_\chi$ . The other parameters are fixed as in Table 3.

singlet dark matter region (defined as  $m_\chi \leq 100$  GeV). In the plot, we observe a funnel region near  $m_\chi \simeq m_h/2$  where the dark matter resonant annihilation occurs via the lightest CP-even Higgs with mass 125 GeV. The dominant processes contributing to the relic density in this region are  $b\bar{b}$  and sub dominant contributions from  $WW$ . As one moves away from the funnel region, the  $WW$  mode starts dominating over  $b\bar{b}$ . This is due to the increasing phase space available to the final state particles due to the increase in mass of the dark matter candidate in the initial states. This continues upto masses close to  $m_W$  while near  $m_\chi \simeq m_W$ , the dominating mode is  $WW$ . As one increases  $m_\chi$  further the  $ZZ$  mode is now allowed once the  $m_\chi \simeq m_Z$ . In this

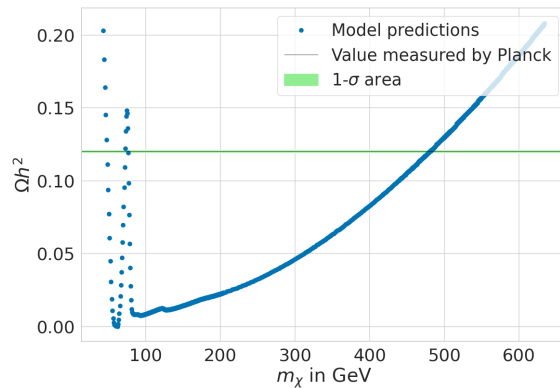


**Figure 5.** Relic density predicted by the model depending on the DM mass  $m_\chi$ . The parameter  $m_S^2$  is varied in this plot in the range given in Table 4. The other input parameters are fixed as in Table 3.

region both the  $WW$  and  $ZZ$  modes contribute to the relic density computation. As  $m_\chi \simeq m_h$ , the di-Higgs channel opens up. Further, for  $m_\chi \simeq m_t$  allows for  $t\bar{t}$  channel to open up.

We also look into the high mass region ( $m_\chi > 100$  GeV) with a large portion of the parameter space remains underabundant until  $\simeq 480$  GeV after which the dark matter overcloses the universe. The processes contributing to the relic density are summarised in the Fig. 1. We observe that in these regions as discussed the dominant modes are  $WW$ ,  $t\bar{t}$ ,  $hh$ ,  $ZZ$ .

### Direct detection

The relevant constraint from direct detection cross section of dark matter arises from the spin-independent (SI) interactions. The variation of the direct detection cross section is plotted against the dark matter mass  $m_\chi$ . We choose the parameters for the singlet and 2HDM parameters as in **BPA** and vary  $m_S^2$  to vary the dark matter mass for  $\tan\beta = 5$ . We observe the dark matter direct detection stringently rules out dark matter masses less than 100 GeV while heavy dark matter remains allowed by current data.

### Case A: Light singlet dark matter

There is a rapid change observed in the relic density near the  $Z$  boson threshold where the thermal relic density is achieved. We focus on this region of light singlet dark matter region (defined as  $m_\chi \leq 100$  GeV). Fig. 8 shows the variation of the relic density with the dark matter mass in this region. In this Higgs funnel region the dominant processes contributing to the relic density in this Higgs funnel region are  $b\bar{b}$ ,  $gg$ ,  $\tau\bar{\tau}$ . As one moves to higher masses, the  $b\bar{b}$  mode decreases while the

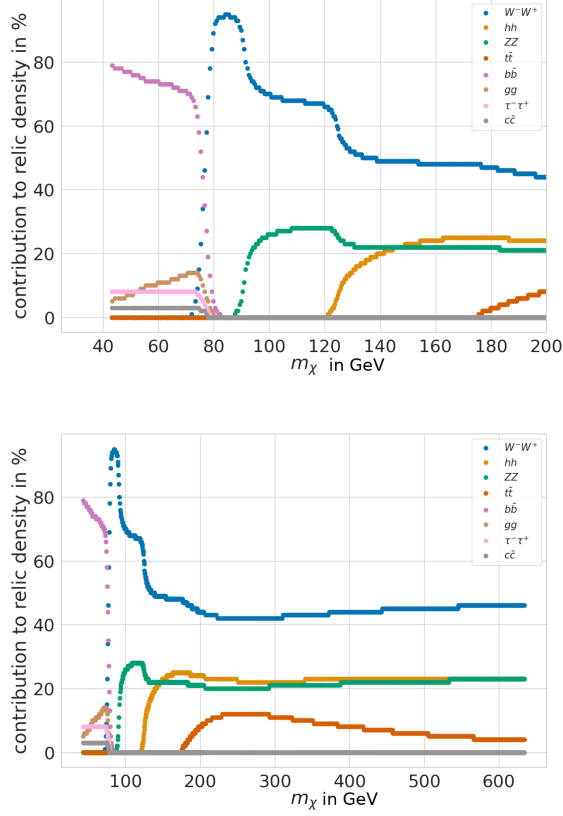


**Figure 6.** The different processes contributing to the relic density.

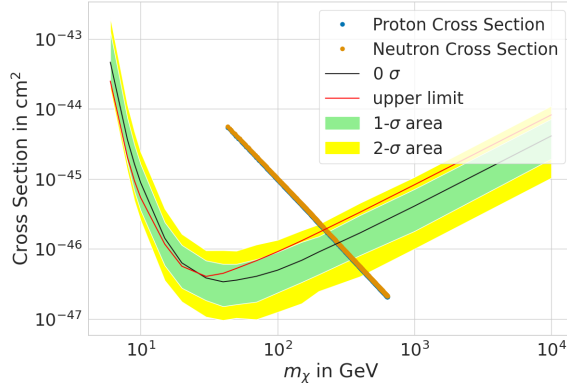


**Figure 7.** Variation of the direct detection cross-section against mass of the dark matter candidate. The parameter  $m_S^2$  is varied in this plot in the range given in Table 4. The other input parameters are fixed as in Table 3.

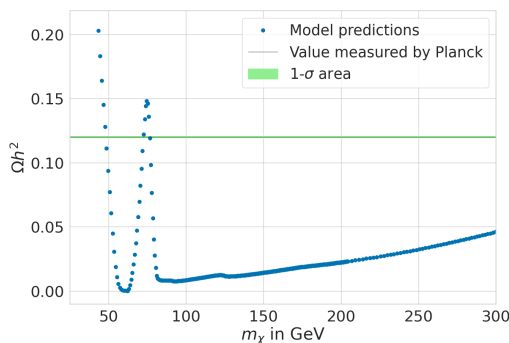


**Figure 8.** Rapidly changing relic density in low DM mass region. The parameter  $m_S^2$  is varied in this plot in the range given in Table 4. The other input parameters are fixed as in Table 3.

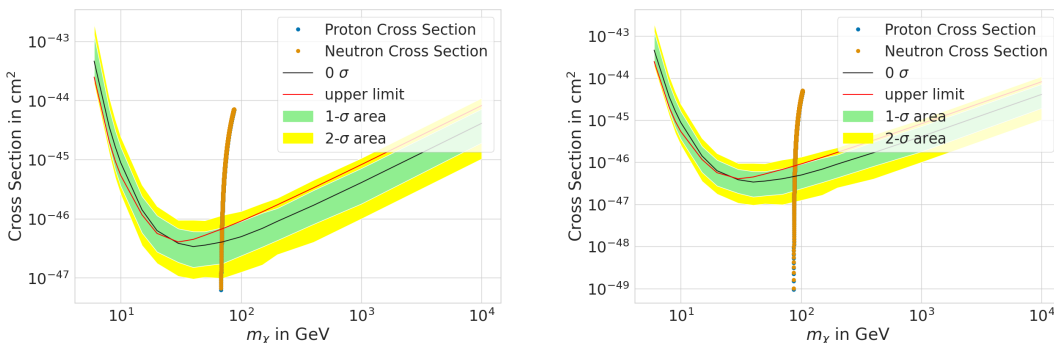


**Figure 9.** Variation of the direct detection cross-section with mass of the DM for varying  $\lambda'_2$  for two values of  $\tan \beta = 5, 20$ . The parameters varied in this plot is  $\lambda'_2$  as in the Table 5 while the other parameters are same as in Table 3.

$WW$  mode opens up as seen in the top panel of Fig. 6. However from Fig. 7 such a region is observed to be ruled out from the direct detection data. We now vary the other singlet parameters to see their effect on the direct detection parameters.

| Parameters | $\lambda'_2$    | $\tan \beta$ | $m_S^2(\text{GeV}^2)$ |
|------------|-----------------|--------------|-----------------------|
| Values     | $10^{-4} - 0.1$ | 5,20         | 4200                  |

**Table 5.** List of parameters for the variation of relic density and direct detection cross-section with  $m_\chi$  for varying  $\lambda'_2$  for two values of  $\tan \beta$ . The other input parameters are as in Table 3.

The strongest effect occurs of the portal coupling parameter  $\lambda'_2$  and  $\tan \beta$ . This can be explained from the nature of the coupling  $\lambda_{hSS^*}$  and  $\lambda_{HSS^*}$  (see eq. 2.8 and 2.11

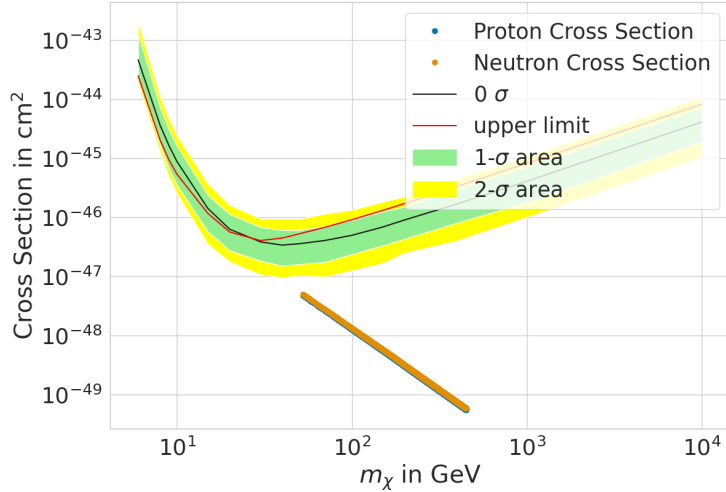


**Figure 10.** Variation of the direct detection cross-section with  $m_\chi$  for  $\lambda'_2 = 0.001$  and  $\tan\beta = 12$ . The scan range for  $m_S^2$  is shown in Table 6 while the other parameters are fixed as in Table 3.

respectively) which in the decoupling limit ( $\sin(\beta - \alpha) \simeq 1$ ) are functions of  $\lambda'_1$ ,  $\lambda'_2$  and  $\tan\beta$ . We observe this behaviour in Fig. 9 demonstrates the effect of using a smaller  $\lambda'_2$  on the direct detection plot for two values of  $\tan\beta = 5, 20$ . As observed from the plot, a large part of the parameter space remains allowed for such small values of  $\lambda'_2$ . We now scan over  $m_\chi$  as in the Table 6 and demonstrate the allowed parameter space in Fig. 10.

| Parameters | $m_S^2$ (GeV <sup>2</sup> ) |
|------------|-----------------------------|
| Values     | 1000-200000                 |

**Table 6.** Scan range for the variation of direct detection cross-section against the DM mass for  $\lambda'_2 = 0.001$  and  $\tan\beta = 12$ . The other parameters are fixed as in Table 3.

### Case B: heavy dark matter regions

From Fig. 6, we observe that the relic density remains underabundant upto  $m_\chi \leq 480$  GeV. From direct detection cross-section constraint in Fig. 7 and 10 is also weakly constrained for the heavy dark matter regions.

In summary, we observe that the relic density is satisfied only around  $m_\chi \simeq 75$  GeV and  $\simeq 480$  GeV. Below 480 GeV, the DM relic density is mostly underabundant with the Higgs resonance region opening up near 62-63 GeV. In this region, the dominant annihilation process of the DM is via the light 125 GeV Higgs with  $b\bar{b}$

being the dominant annihilation process. For heavier masses, the  $WW$  process is the dominant process especially near the 75 GeV mass peak. In the following sections, we look into differences between real and complex scalar dark matter and some representative benchmarks consistent with experimental constraints including dark matter, flavour physics, Higgs sector and collider constraints on heavy Higgses.

## 6 Distinguishing between real and complex scalar dark matter

In this section, we investigate the differences between a real and complex singlet scalar dark matter in the context of 2HDMS. Similar comparison has been previously studied for the SM with singlet extensions[2] and for the 2HDM + scalar/pseudoscalar DM [36] in the context of collider signals.

The real scalar singlet extended 2HDM potential is

$$V_{RS} = M_{RS}^2 S^2 + \frac{\lambda''_{R3}}{4} S^4 + S^2[\lambda'_{1R} \Phi_1^\dagger \Phi_1 + \lambda'_{2R} \Phi_2^\dagger \Phi_2]$$

In the real scalar limit of the complex scalar potential in Eq. 2.1, the parameters are related as

$$\begin{aligned} M_{RS}^2 &= m_S^2 + m_S'^2 \\ \lambda''_{3R} &= \lambda''_3 + \frac{5}{3} \lambda''_1 \\ \lambda'_{1R} &= \lambda'_1 + 2\lambda'_4 \\ \lambda'_{2R} &= \lambda'_2 + 2\lambda'_5 \end{aligned}$$

In the limit of real  $S$ , the complex scalar potential also reduces to the form of a real scalar potential for  $m_S'^2, \lambda'_4, \lambda'_5, \lambda''_1 = 0$ ,

$$\begin{aligned} M_{RS}^2 &= m_S^2 \\ \lambda''_{3R} &= \lambda''_3 \\ \lambda'_{1R} &= \lambda'_1 \\ \lambda'_{2R} &= \lambda'_2 \end{aligned}$$

The results using the input parameters as in **BPA** is summarised in Table 7. The processes contributing to the relic density  $WW$  (44%),  $hh$ (24%),  $ZZ$ (22%) and  $t\bar{t}$  (10%). In Table 8 we summarise all the cases discussed so far. We observe that for the same value of input parameters, the relic density in the real scalar case is larger than the complex case while the direct detection cross-section remains the same.

We now perform a scan using the parameters listed in **BPA** for comparison between the two cases. We fix the same mass for the dark matter candidate and the

| Parameters                     | <b>BPB</b>             |
|--------------------------------|------------------------|
| $M_{RS}^2$ (GeV <sup>2</sup> ) | 1.13e+05               |
| $\lambda''_{3R}$               | 0.1                    |
| $\lambda''_{1R}$               | 0.042                  |
| $\lambda''_{2R}$               | 0.042                  |
| $m_\chi$ (GeV)                 | 338.9                  |
| $m_h$ (GeV)                    | 124.99                 |
| $m_H$ (GeV)                    | 724.4                  |
| $m_A$ (GeV)                    | 724.4                  |
| $m_{H^\pm}$ (GeV)              | 728.3                  |
| $\Omega h^2$                   | 1.2                    |
| $\sigma_{SI}^P$ (in pb)        | $7.67 \times 10^{-11}$ |
| $\sigma_{SI}^N$ (in pb)        | $7.90 \times 10^{-11}$ |

**Table 7.** The benchmark point in the real singlet extended 2HDM.

| Benchmark  | $\Omega h^2$ | $\sigma_p^{SI}$ (in pb) | $\sigma_n^{SI}$ (in pb) |
|------------|--------------|-------------------------|-------------------------|
| <b>BPA</b> | 0.059        | 7.65e-11                | 7.88e-11                |
| <b>BPB</b> | 1.20         | 7.67e-11                | 7.90e-11                |

**Table 8.** Comparison of the DM observables for **BPA** for both complex and real scalar DM.

Higgs spectrum in both cases. We also ensure the same portal couplings  $\lambda'_1$ ,  $\lambda'_2$  and  $\lambda''_3$  in both real and complex cases.

In Fig. 11, we observe the relic density for the same dark matter mass and with same portal couplings is much larger for the real DM case than the complex DM case. The extra contribution to the relic density arising from the processes involving the extra portal and self couplings of the dark matter leads to the different exclusion limits in the complex DM model. We also compare the direct detection cross-section in the plot and observe no differences for the real limit of the complex case. This can be attributed to the fact that only the portal couplings  $\lambda'_1$  and  $\lambda'_2$  contribute in both cases for conserved DM number.

## 7 Benchmarks

We now choose some representative benchmark regions for our model consistent with all experimental constraints. We choose benchmark points in the light and heavy dark matter regions and also the possibility of the decay of the Higgses to the dark matter candidate as summarised in Table 9. The model is implemented in SARAH[35]

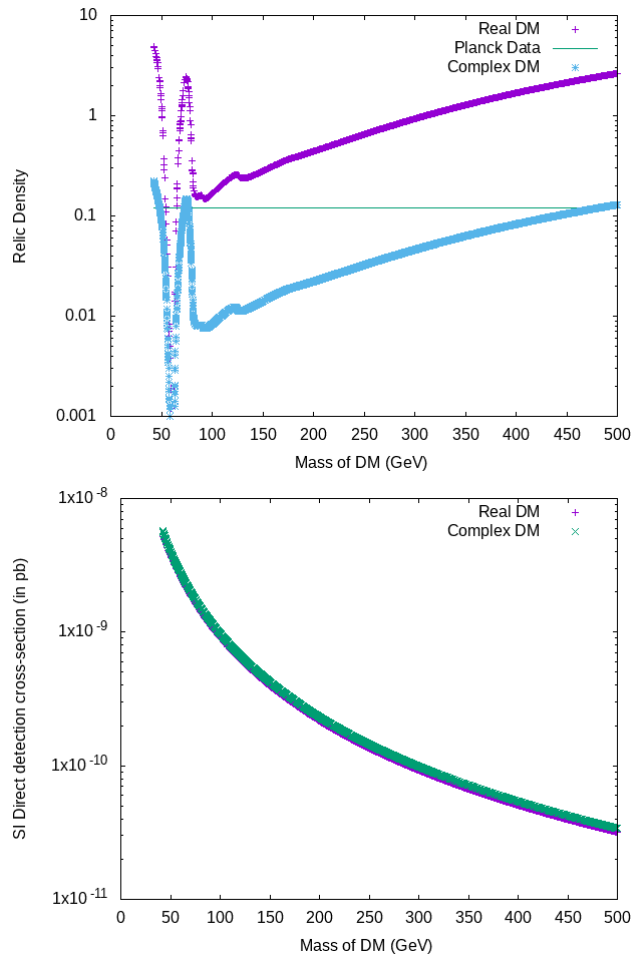


**Figure 11.** Relic density (left) and SI (spin-independent) direct detection cross-section (right) for real and complex DM.

and `SPheno-v4.0.4`[34] is utilised to obtain the benchmarks for the study. The tree level unitarity constraints are checked using `SPheno-4.0.4`. In the following analysis `micrOMEGAs-v5.2.4`[32] is used to compute the tree-level relic density and DM-nucleon cross-sections. The constraints from the Higgs sector are checked using `HiggsBounds-v5`[37] and `HiggsSignals-v2`[38] at tree-level.

Benchmark **BP1** with 125 GeV lightest CP-even Higgs as in Table 9. The relic density  $\Omega h^2 = 0.059$  and the direct detection cross section,  $\sigma_{DD} = 7.55 \times 10^{-11}$  pb. The benchmark has an underabundant relic density but is consistent with the DM constraints from PLANCK as well as the XENON1T data for DM-nucleon scattering cross-sections. The dominating annihilation channels are into  $W^+W^-$  (43%),  $hh$  (22%),  $ZZ$ (21%) and  $t\bar{t}$ (10%). This benchmark represents a heavy DM case and with the Higgs sector which is 2HDM-like such that there are no appreciable decays to the dark matter.

| Parameters                          | <b>BP1</b>         | <b>BP2</b>         | <b>BP3</b>         |
|-------------------------------------|--------------------|--------------------|--------------------|
| $\lambda_1$                         | 0.23               | 0.1                | 0.23               |
| $\lambda_2$                         | 0.25               | 0.26               | 0.26               |
| $\lambda_3$                         | 0.39               | 0.10               | 0.2                |
| $\lambda_4$                         | -0.17              | -0.10              | -0.14              |
| $\lambda_5$                         | 0.001              | 0.10               | 0.10               |
| $m_{12}^2(\text{GeV}^2)$            | $-1.0 \times 10^5$ | $-1.0 \times 10^5$ | $-1.0 \times 10^5$ |
| $\lambda_1''$                       | 0.1                | 0.1                | 0.1                |
| $\lambda_3''$                       | 0.1                | 0.1                | 0.1                |
| $\lambda_1'$                        | 0.042              | 0.04               | 2.0                |
| $\lambda_2'$                        | 0.042              | 0.001              | 0.01               |
| $\lambda_4'$                        | 0.1                | 0.1                | 0.1                |
| $\lambda_5'$                        | 0.1                | 0.1                | 0.1                |
| $m_h$ (GeV)                         | 125.09             | 125.09             | 125.09             |
| $m_H$ (GeV)                         | 724.4              | 816.4              | 821.7              |
| $m_A$ (GeV)                         | 724.4              | 812.6              | 817.9              |
| $m_{H^\pm}$ (GeV)                   | 728.3              | 816.3              | 822.2              |
| $\tan \beta$                        | 4.9                | 6.5                | 6.5                |
| $m_{DM}$ (GeV)                      | 338.0              | 76.7               | 323.6              |
| $\Omega h^2$                        | 0.058              | 0.119              | 0.05               |
| $\sigma_{SI}^p \times 10^{10}$ (pb) | 0.76               | 0.052              | 2.9                |
| $\sigma_{SI}^n \times 10^{10}$ (pb) | 0.78               | 0.054              | 3.1                |

**Table 9.** Relevant parameters of the benchmark used for the study. All mass parameters have units GeV except for  $m_{12}^2$  in  $\text{GeV}^2$ . The decimal points are rounded to the first decimal place for the masses and upto the third decimal place for relic density, and direct detection cross-sections.

**BP2** with  $m_\chi = 76.6$  GeV is another benchmark addressing the light dark matter region which passes all the constraints from the Higgs signal strength to ensure a phenomenologically viable benchmark point.

For both **BP1** and **BP2**, the dominant decay modes of the Higgses are summarised in Table 10. In this case, the invisible branching is suppressed and the Higgses decay only with the 2HDM decay modes therefore is completely indistinguishable with respect to the 2HDM. In presence of the dark matter, there are additional decay channels opening up for the heavy Higgs,  $H \rightarrow \chi\bar{\chi}$ . The presence of the invisible DM candidate in the final state ensures the presence of missing energy in the final state signal at colliders. Such signatures have been recently studied with the heavy Higgs as a portal to dark matter and its collider signals of mono-jet and VBF along with missing transverse energy at the LHC[8]. We consider this case in **BP3**

where the allowed invisible branching of the Higgses is  $\sim 4.8\%$  and all experimental constraints are respected. **BP3** is also a heavy DM benchmark point where the dark matter mass  $\sim 324$  GeV and is allowed by direct detection data at 90% confidence level (CL). We also observe that the invisible decay branching of the Heavy Higgs in **BP3** is severely constrained from direct detection searches.

| Decay Channels                         | Branching ratios for |            |            |
|--|----------------------|------------|------------|
|  | <b>BP1</b>           | <b>BP2</b> | <b>BP3</b> |
| $H \rightarrow b\bar{b}$               | 0.14                 | 0.29       | 0.24       |
| $H \rightarrow t\bar{t}$               | 0.83                 | 0.66       | 0.68       |
| $H \rightarrow \tau\bar{\tau}$         | 0.02                 | 0.45       | 0.04       |
| $H \rightarrow \chi\bar{\chi}$         | 0.0                  | 0.0        | 0.05       |
| $A \rightarrow b\bar{b}$               | 0.12                 | 0.27       | 0.27       |
| $A \rightarrow t\bar{t}$               | 0.86                 | 0.69       | 0.69       |
| $A \rightarrow \tau\bar{\tau}$         | 0.02                 | 0.04       | 0.04       |
| $H^\pm \rightarrow t\bar{b}$           | 0.97                 | 0.96       | 0.96       |
| $H^\pm \rightarrow \tau\bar{\nu}_\tau$ | 0.022                | 0.03       | 0.03       |

**Table 10.** The branching ratios for the dominant decay modes of the heavy Higgses for the benchmarks **BP1**, **BP2** and **BP3**. The branching ratios are rounded up to the second decimal place.

## 8 Collider Analysis

In this section, we discuss the potential signals of this model at HL-LHC and future  $e^+e^-$  colliders. As discussed in the previous section, the presence of the invisible decay of the heavy Higgs to the dark matter candidate is a source of missing energy at colliders. Therefore, direct production of heavy Higgses and consequent decay of the Higgs to  $\chi$  along with visible SM particles can give rise to distinct signatures for this scenario as opposed to the 2HDM like scenario. We investigate these possibilities further in the following sub-sections and discuss their prospects in the context of  $\sqrt{s} = 14$  TeV LHC at the targeted integrated luminosity of 3-4  $\text{ab}^{-1}$  and in future  $e^+e^-$  colliders upto  $\sqrt{s} = 3$  TeV and integrated luminosities 5  $\text{ab}^{-1}$ . We also briefly summarise the simulation set-up for our analysis below.

### Simulation details

We use `MG5_aMC_v3_1_1` [39, 40] to generate the parton level processes for both signal and background samples. For hadronisation and showering, `Pythia-8`[41] is used while the detector simulation is performed using `Delphes-v3.4.1` [42–44] using the default Delphes cards provided for **ATLAS** for the LHC study and the default card for

the ILD detector for the  $e^+e^-$  study. We performed the signal background analysis for LHC using `Delphes` while the analysis for the electron-positron collider is performed using `Madanalysis-v5`[45–49].

### 8.1 Prospects at LHC

The main processes contributing to neutral Higgs production are gluon fusion (mediated by the top quark loop), vector boson fusion (VBF), associated Higgs production ( $Vh_i$ ),  $b\bar{b}h_i$ ,  $t\bar{t}h_i$ [4]. For the charged Higgs pair, the possible production channels are  $H^+H^-$  and  $W^\pm H^\mp$  [4]. At LHC Run 3 at  $\sqrt{s} = 14$  TeV, all possible Higgs production processes (including SM and BSM Higgses) are summarised in Table 11 for **BP1**. From the Table 11, we see HL-LHC running at 3-4  $\text{ab}^{-1}$  is necessary to have a through

| Processes     | Cross section (in fb) at<br>$\sqrt{s} = 14$ TeV |
|---------------|---|
| $h$ (ggF)     | $29.3 \times 10^3$                              |
| $H$           | 22  |
| $A$           | 35  |
| $hjj$ (VBF)   | $1.296 \times 10^3$                             |
| $Hjj$         | 1.843   |
| $Ajj$         | 2.885   |
| $Wh$          | $1.148 \times 10^3$                             |
| $WH$          | $1.195 \times 10^{-3}$                          |
| $WA$          | $4.3 \times 10^{-4}$                            |
| $Zh$          | 880.8   |
| $ZH$          | 0.93  |
| $ZA$          | 3.999   |
| $bbh$         | 2.534   |
| $bbH$         | 21.52   |
| $bbA$         | 23.39   |
| $t\bar{t}h$   | 478.3   |
| $t\bar{t}H$   | 0.1988  |
| $t\bar{t}A$   | 0.2552  |
| $H^+H^-$      | $6.603 \times 10^{-2}$                          |
| $W^\pm H^\mp$ | 102.4   |

**Table 11.** The leading order (LO) cross-section (in fb) for dominant processes for **BP1** before analysis for  $\sqrt{s} = 14$  TeV LHC.

collider search for heavy Higgses close to a TeV range. The current constraints on heavy Higgses are summarised in[27, 28]. Projection studies of heavy Higgses predict mass reach of upto TeV for direct detection [50, 51] and indirect detection [52]. The

HL-LHC is important to achieve the required luminosity to observe these channels and gain indirect insight into the BSM Higgs sector. From the benchmark Table 9, we observe that for the case with the H decaying to dark matter particle, di-jet+ $\cancel{E}_T$ , di-lepton+ $\cancel{E}_T$ ,  $b\bar{b} + \cancel{E}_T$  and mono-jet+ $\cancel{E}_T$  are the possible channels to probe this model at hadron colliders. The VBF and gluon fusion channel have been studied for the real singlet at LHC and are good discovery probes[8]. For the mass ranges of the heavy Higgses considered in our study, the dominant production processes at  $\sqrt{s} = 14$  TeV LHC are:  $b\bar{b}H$ ,  $H + jj(ggF)$ ,  $VBF$ ,  $ZH$  and  $t\bar{t}H$ . involving  $WH$  associated production are suppressed due to the suppressed couplings of the heavy Higgses with respect to the SM couplings to the gauge bosons.

In presence of the heavy Higgs  $H$  decaying to two dark matter candidates, one can obtain invisible momentum in the final state. Keeping this in mind, one can look into the following final states:

- $1j$  (ISR)+ $\cancel{E}_T$ [53]
- $2j + \cancel{E}_T$  [54]

We estimate the significance for the mono-jet and VBF channels using the cuts from an existing cut-and-count analyses performed in Ref.[8] for  $\sqrt{s} = 14$  TeV LHC.

### Pre-selection cuts

The cuts used in this paper are summarised below. We choose the Delphes ATLAS card for reference.

- The leptons are reconstructed with a minimum transverse momentum,  $p_T > 10$  GeV and pseudorapidity  $|\eta| < 2.5$  while excluding the transitional pseudorapidity gap between the barrel and the end cap of the calorimeter  $1.37 < |\eta| < 1.52$ .
- Photons are reconstructed with  $p_T > 10$  GeV and  $|\eta| < 2.5$ .
- All jets are reconstructed using  $\Delta R = 0.4$  using the anti- $k_T$  algorithm and minimum  $p_T > 20$  GeV with pseudorapidity  $|\eta| < 2.5$ .

### Signal Region A: $1j + \cancel{E}_T$

In this subsection, we estimate the signal events for the monojet and missing energy channel using the background estimates in Ref. [8]. Using the cuts of  $p_T(j) > 250$  GeV and  $\cancel{E}_T > 250$  GeV, one obtains a cut efficiency for the signal **BP3**  $\sim 18\%$ . For the cut and count analysis, the estimated significance we obtain a  $0.111\sigma$  excess at  $3\text{ab}^{-1}$  using gluon fusion production channel (at leading order (LO)).

## Signal Region B: $2j + \cancel{E}_T$

We study the VBF topology for the signal region consisting of two forward jets and missing energy. We follow the cuts in Ref.[8] for estimating the cut efficiency and use the background estimates from their paper. Using the signal cross-section at LO, we get the a signal efficiency of 4.5% for **BP3** and the signal significance is  $\sim 0.2 \sigma$  at  $3 \text{ ab}^{-1}$ . Therefore, we observe that owing to the small invisible branching ratio and heavy Higgs masses  $\sim 820 \text{ GeV}$  (and hence small production cross-section) in **BP3**, the final states are inaccessible at the upcoming HL-LHC run. We estimate the prospects of observing such a benchmark at the  $e^+e^-$  collider in the following sub-section.

### 8.2 Prospects at $e^+e^-$ colliders

The cleaner environment and lesser background along the beam line compared to hadron colliders make the electron positron linear colliders an attractive choice for precision studies of new physics. The International Linear Collider (ILC)[55], is a proposed  $e^+e^-$  collider with center-of-mass energies at the SM-like Higgs threshold ( $\sqrt{s} = 250 \text{ GeV}$ ), top threshold ( $\sqrt{s} = 350 \text{ GeV}$ ) and further upgrades such that the center of mass energies are  $\sqrt{s} = 500 \text{ GeV}$  and upto  $\sqrt{s} = 1 \text{ TeV}$  with a maximum target integrated luminosity of  $\mathcal{L} = 500 \text{ fb}^{-1}$ . ILC gains advantage over the LHC in the possibility of exploiting the polarisation of the electron and positron beams leading to increased background suppression[56]. Other proposed  $e^+e^-$  colliders are CLIC [57, 58] with an energy upgrade upto  $\sqrt{s} = 1.5, 3 \text{ TeV}$ , FCC-ee [59] and CEPC [60] with the latter having beam energies upto the  $t\bar{t}$  threshold. For an  $e^+e^-$  collider, the main processes contributing to neutral Higgs production are  $Zh$ ,  $b\bar{b}h$ ,  $\nu\bar{\nu}h$ [4]. For the heavy scalar  $H$  and pseudoscalar  $A$ , the only relevant production channel which would be accessible upto  $\sqrt{s} = 3 \text{ TeV}$  are  $b\bar{b}H$ ,  $b\bar{b}A$ ,  $hA$ ,  $HA$ ,  $t\bar{t}H/A$  and  $\nu\bar{\nu}H/A$ . For the charged Higgs pair, the possible production channels are  $H^+H^-$  and  $W^\pm H^\mp$ [4]. One has the possibility of accessing the heavy Higgses via the channels  $b\bar{b}H/A$ ,  $HA$  and  $t\bar{t}H/A$  at the CLIC with  $\sqrt{s} = 1.5(3) \text{ TeV}$  with an integrated luminosity up to  $500 \text{ fb}^{-1}$  for ILC and up to  $5 \text{ ab}^{-1}$  for the CLIC. As a representative study, we perform a signal-background analyses at a generic  $e^+e^-$  collider with  $\sqrt{s} = 3 \text{ TeV}$  and unpolarised electrons and positrons to assess the observability of these channels after background rejection for **BP3**. Presence of the invisible dark matter in the final state manifests as missing energy in the final state along with visible SM-particles such as  $(b)$ -jets,  $e/\mu/\tau$  leptons from the pseudoscalar decay which we investigate further in the collider analysis.

### Signals and backgrounds

From Table 10, we observe that the dominant decay of the pseudoscalar are to a pair of top quarks and  $b$  quarks, and for **BP3** a smaller fraction of the CP-even

heavy Higgs decays to the dark matter which manifests itself as missing energy in the collider. In such cases of invisibly decaying heavy CP-even Higgs, production processes such as  $HA$ ,  $b\bar{b}H$ ,  $t\bar{t}H$  and  $ZH$  lead to final states including (at least) two b-jets and missing energy while  $Hjj$  leads to a final state with two light jet associated with the missing energy with the latter having a VBF topology. On the other hand, production channel  $\nu\bar{\nu}H$  state leads to a fully invisible state which in order to be probed requires an ISR photon against which the invisible system recoils. Besides, note that the heavy Higgses ( $A$ ) also decay to a pair of tau leptons, therefore allowing final state of  $2\tau + \cancel{E}_T$  from  $HA$  production channel. Since the branching ratio of the  $A$  are dominantly into  $t\bar{t}$  followed by  $b\bar{b}$  one expects final states involving at least  $2b + \cancel{E}_T$  to be dominant over the tau final states. We look into the prospects of observing signals including  $2b + \cancel{E}_T$ . We leave the study of the tau and photon final states as a future study. Therefore the relevant signal processes consists of the following production channels of the heavy CP-even Higgs,  $H$  such as

$$e^-e^+ \rightarrow HA, b\bar{b}H, t\bar{t}H$$

Contributions from  $HA, b\bar{b}H, t\bar{t}H$  lead to the final state of  $2b + \cancel{E}_T$  with the missing energy arising from  $H \rightarrow \chi\bar{\chi}$  while contributions from  $ZH$  production cross-section is considerably suppressed at  $\sqrt{s} = 3$  TeV upto integrated luminosity of  $\mathcal{L} = 5$  ab $^{-1}$ .

### Pre-selection cuts

The cuts used for identifying the reconstructed objects after reconstruction with the default ILD card in `Delphes` are summarised below and denoted as **C0**,

- Leptons are reconstructed with a minimum transverse momentum,  $p_T > 10$  GeV and pseudorapidity  $|\eta| < 2.5$ .
- Photons are reconstructed with  $p_T > 10$  GeV and  $|\eta| < 2.5$ .
- All (b)-jets are identified with minimum  $p_T > 20$  GeV with pseudorapidity  $|\eta| < 3.0$ .

### Signal Region C: $2b + \cancel{E}_T$

We investigate the prospects of the final state consisting of two b-jets along with missing energy. Dominant contributions arise from

- $b\bar{b}$  (for misidentification of decay products of  $b$ -quark along with missing energy from  $b$  decays)
- $b\bar{b}\nu\bar{\nu}$  (including both on-shell and off-shell contribution from  $Z$  boson decay as well as  $\nu\bar{\nu}h$  contribution)
- $Z(\rightarrow \ell^+\ell^-)Z(\rightarrow \nu\bar{\nu})$

- $hZ$  ( $h \rightarrow b\bar{b}, Z \rightarrow \nu\bar{\nu}$ )
- $t\bar{t}Z$ , ( $Z \rightarrow \nu\bar{\nu}, t \rightarrow bW^+$ ) for misidentified leptons/jets from  $W$  bosons.
- Leptonic  $t\bar{t}$  for misidentified leptons or semi-leptonic  $t\bar{t}$  decays with missing energy arising from the  $b$  decaying leptonically.
- $WWZ$
- $ZZZ$

| Process                    | Production cross-section (in fb) |
|----------------------------|----------------------------------|
| $HA$                       | 0.0341                           |
| $b\bar{b}H$                | 0.0231                           |
| $t\bar{t}H$                | 0.0202                           |
| $ZZ$                       | 1.54                             |
| $WW$                       | 22.12                            |
| $b\bar{b}\nu\bar{\nu}$     | 40.84                            |
| $b\bar{b}$                 | 10.17                            |
| $t\bar{t}$ (leptonic)      | 0.87                             |
| $t\bar{t}$ (semi-leptonic) | 5.2                              |
| $t\bar{t}Z$                | 0.0149                           |
| $hZ$                       | 0.23                             |
| $WWZ$                      | 0.23                             |
| $ZZZ$                      | 0.0151                           |

**Table 12.** Production cross sections (in fb) for the signal processes at  $\sqrt{s} = 3$  TeV for **BP3** (with  $H \rightarrow \chi\bar{\chi}$ ) and SM backgrounds (with leptonic decay for tops,  $W$  boson, invisible decay of  $Z$ ,  $Z \rightarrow b\bar{b}$  and  $h \rightarrow bb$ ).

For the backgrounds such as  $t\bar{t}, t\bar{t}Z$  we generate the leptonic mode. For the other SM backgrounds:  $Z(\rightarrow b\bar{b})Z(\rightarrow \nu\bar{\nu}), h(\rightarrow b\bar{b})Z(\rightarrow \nu\bar{\nu}), W(l\nu)W(l\nu)Z(\rightarrow b\bar{b})$  modes are generated. Since the signal benchmark **BP3** has a large dark matter mass ( $m_\chi \simeq 323$  GeV), with the DM candidate originating from the decay of the heavy Higgs  $H$  and a large mass gap between the parent and daughter particles, the signal sample has a large missing transverse energy as seen in Fig. 12 for the 2 b-jet final state. In order to generate the irreducible background final state  $b\bar{b}\nu\bar{\nu}$ , a large  $\cancel{E}_T (> 350$  GeV) to tame the large the cross-section of this background. The signal and background production cross-section in the missing energy final state are summarised in Table 8.2. We now perform a signal background analyses using the cuts **C1-C6** as follows,

- **C1:** The final state consists of two b-jets and no leptons or photons.

- **C2**: The leading b-jet has transverse momentum  $p_T > 100$  GeV and sub-leading b-jet has  $p_T > 80$  GeV. The hard  $p_T$  cuts on the b-jets help reduce backgrounds from SM backgrounds from  $Z$  and  $h$  bosons.
- **C3**: The invariant mass of the two b-jets within the mass window  $80 < M_{b_1 b_2} < 130$  is rejected to remove contributions from  $Z$  and  $h$  bosons.
- **C4**: Since the dark matter is heavy, we demand a large cut on the effective mass  $M_{eff} > 1.2$  TeV where  $M_{eff} = \sum_i(p_{T_i}) + \cancel{E}_T$ .
- **C5**: Further, the large mass-gap between the heavy Higgs and the dark matter allows for a large missing energy. We demand  $\cancel{E}_T > 650$  GeV on the final state which reduces the dominant SM backgrounds.
- **C6**: The  $\Delta\Phi$  between two b-jets is significantly different for the signal and background from  $b\bar{b}$  where the b-jets are mostly back-to-back. We demand  $\Delta\Phi(b_1, b_2) < 1.60$ . This also reduces the backgrounds from  $b\bar{b}$  as well as from  $t\bar{t}$  and  $t\bar{t}Z$  sharply.

The number of signal and background events after applying the cuts **C1-C6** (at  $\mathcal{L} = 5 \text{ ab}^{-1}$ ) are summarised in Table 13. We observe that the large  $M_{eff}$  and  $\cancel{E}_T$  cut are instrumental in reducing SM backgrounds sharply. Further, the variable  $\Delta\Phi(b_1, b_2)$  also reduces contributions from  $b\bar{b}$  owing to the fact that the jets in the background are back to back while in the signal they are more collimated. It also reduces the backgrounds from  $t\bar{t}$  and  $t\bar{t}Z$  sharply which are also peaked towards higher values of  $\Delta\Phi$  as compared to the signal. We also plot the invariant mass of the two b-jets in Fig. 13 and observe that the SM backgrounds from  $Z$  and  $h$  are peaked at the resonance masses but for the signal the peak is more broad since the parent particle is heavy. However the irreducible background  $b\bar{b}\nu\bar{\nu}$  has a similar shape compared to the signal. Therefore, excluding the mass window  $80 < M_{b_1 b_2} < 130$  removes the resonant backgrounds from  $Z$  and  $h$  bosons however retaining backgrounds involving b-jets associated with neutrinos and also from  $t\bar{t}$  associated backgrounds.

We discuss the signal significance for the unpolarised electron and positron beams. The statistical significance ( $\mathcal{S}$ ) of the signal ( $s$ ) over the total SM background ( $b$ ) is calculated using [61, 62]

$$\mathcal{S} = \sqrt{2 \times \left[ (s + b) \ln\left(1 + \frac{s}{b}\right) - s \right]}. \quad (8.1)$$

where  $s$  and  $b$  are the total signal and background event numbers after the cuts **C1-C6**. We use this expression for the statistical significance as is relevant in this case since the background events are not overwhelmingly large compared to the signal and the limit  $b \gg s$  is not fully accurate.<sup>4</sup> We observe that for **BP3**, although the

<sup>4</sup>In the limit  $b \gg s$ , Eq. 8.1 reduces to  $S = \frac{s}{\sqrt{b}} \simeq 4.21 \sigma$ . Also, for  $S = \frac{s}{\sqrt{s+b}} \simeq 3.63$ .

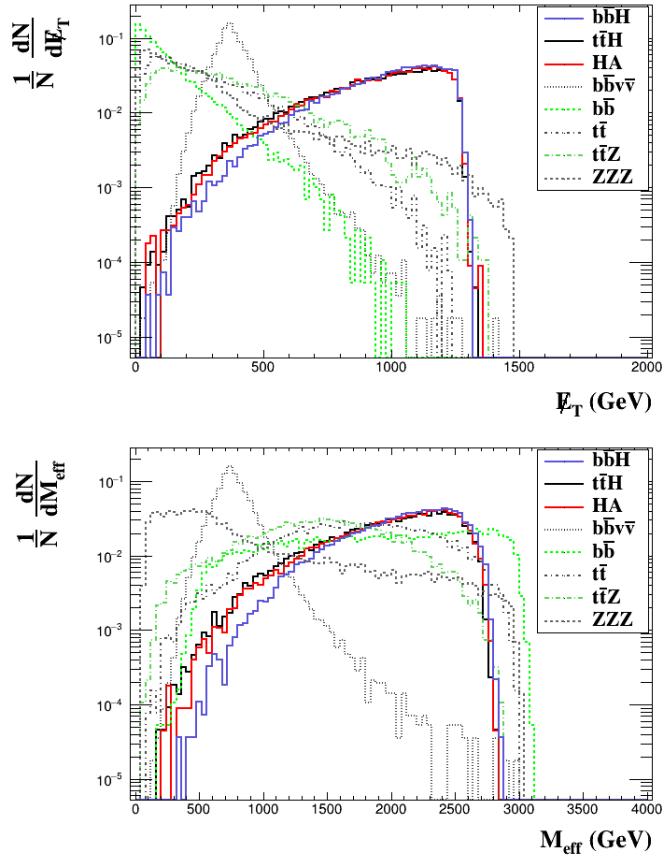


**Figure 12.** Normalized distribution of missing transverse energy( $E_T$ ) and effective mass( $M_{\text{eff}}$ ) for signal vs. some backgrounds after cut **C1**. The  $t\bar{t}$  background here is the leptonic  $t\bar{t}$  contribution.

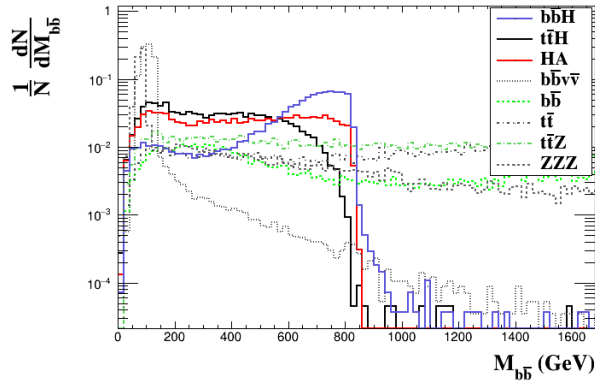


**Figure 13.** Normalized distribution of the invariant mass of the two b-jets for signal vs. background after cut **C1**. The  $t\bar{t}$  background here is the leptonic  $t\bar{t}$  contribution.

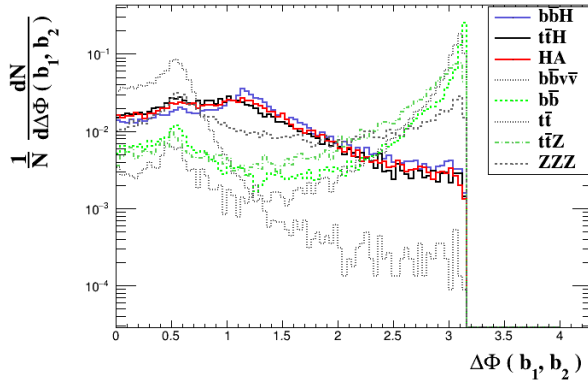


**Figure 14.** Normalized distribution of  $\Delta\Phi$  separation between the two final state b-jets after cut **C1**. The  $t\bar{t}$  background here is the leptonic  $t\bar{t}$  contribution.

invisible decay branching ratio of the heavy Higgs is small, i.e,  $H \rightarrow \chi\bar{\chi} \sim 4.8\%$ , one can obtain  $\sim 4\sigma$  signal at the integrated luminosity of  $5 \text{ ab}^{-1}$ . Note that we have

| Process                    | <b>C0</b> | <b>C1</b> | <b>C2</b> | <b>C3</b> | <b>C4</b> | <b>C5</b> | <b>C6</b> |
|----------------------------|-----------|-----------|-----------|-----------|-----------|-----------|-----------|
| $b\bar{b}H$                | 115       | 32        | 27        | 26        | 26        | 25        | 21        |
| $t\bar{t}H$                | 101       | 22        | 13        | 12        | 12        | 11        | 10        |
| $HA$                       | 170       | 38        | 28        | 24        | 24        | 22        | 20        |
| <b>BP3</b>                 | 51        |           |           |           |           |           |           |
| $b\bar{b}\nu\bar{\nu}$     | 204200    | 35159     | 15738     | 2040.9    | 330.3     | 147.6     | 124.3     |
| $b\bar{b}$                 | 50850     | 9514.5    | 8432.5    | 8387.2    | 6697.5    | 65.6      | 4.07      |
| $ZZZ$                      | 75        | 10.89     | 3.75      | 3.07      | 1.5       | 0.51      | 0.28      |
| $WWZ$                      | 1163      | 42.8      | 3.14      | 1.1       | 0.14      | 0.02      | -         |
| $t\bar{t}Z$                | 74        | 7.1       | 5.68      | 5.6       | 4.04      | 0.71      | 0.35      |
| $t\bar{t}$ (semi-leptonic) | 25955     | 3846.1    | 2843.9    | 2818.8    | 2500.6    | 338.5     | 16.61     |
| $t\bar{t}$ (leptonic)      | 4328      | 565.4     | 481.5     | 478.3     | 401.9     | 29.65     | 1.13      |
| $WW$                       | 110620    | 0.55      | 0.28      | 0.28      | -         | -         | -         |
| $hZ$                       | 1131      | 6.8       | 1.26      | 0.023     | -         | -         | -         |
| $ZZ$                       | 7699      | 167.9     | 42.81     | 13.0      | -         | -         | -         |
| Total background           | 146.4     |           |           |           |           |           |           |
| Significance               | 3.99      |           |           |           |           |           |           |

**Table 13.** The cut-flow table showing the change in the number of events for for benchmark **BP3** for the unpolarised electron and positron at  $\sqrt{s} = 3 \text{ TeV}$  at  $\mathcal{L} = 5 \text{ ab}^{-1}$ . The cuts (**C0-C6**) are defined in the text in sec. 8.2. The '-' represent less than 1 event at integrated luminosity  $\mathcal{L} = 5 \text{ ab}^{-1}$ .

used unpolarised incoming beams for this study. It has been observed that the use of

a right-handed electron and left-handed positron beam polarisation can significantly suppress SM backgrounds [56] and can be effectively used to improve the signal significance as proposed in the upcoming ILC with the possibility of achieving beam polarisations ( $\pm 80\%$ ,  $\mp 30\%$ ) for  $(e^-, e^+)$ . With the CLIC experiment potentially targetting higher center-of-mass energies along with electron polarisation, one may hope to improve upon the signal significance further.

## 9 Summary and Conclusions

In this work, we consider the Two Higgs Doublet model extended with a complex singlet scalar (2HDMS) which is motivated from the possibility of addressing multiple open issues in Nature such as dark matter, baryogenesis and CP-violation. In this work, we focus on the dark matter aspect with the complex scalar singlet as the dark matter candidate. Since the scalar does not develop a vacuum expectation value, the Higgs spectrum is the same as in 2HDM. We focus on a Type II softly broken  $Z_2$  symmetric 2HDM scalar potential augmented with a complex scalar symmetric under  $Z'_2$  stabilizing the dark matter candidate. In the CP-conserving scenario, the CP-even Higgses act as a portal to the dark matter. We explore the allowed parameter space allowed by current experimental data from dark matter, flavour physics and collider constraints from the SM-like Higgs as well as searches for the heavy Higgses and choose some representative benchmarks for light and heavy dark matter mass region are chosen. We observe that direct detection results stringently constrain the parameter space and therefore requiring low values of  $\lambda'_2$ . Further, we compare our results to the real singlet extended 2HDM and observe that the relic density is much larger for the complex scalar DM over real scalar DM while the direct detection cross-section remains unchanged.

Presence of the singlet also leads to new decay modes for the Higgses with the Higgses decaying to a pair of dark matter particles. Such a final state will lead to the presence of missing energy at colliders. We choose a benchmark **BP3** with  $m_H \simeq 820$  GeV consistent with all experimental data in order to demonstrate the prospects of observing such a signal at LHC and future  $e^+e^-$  colliders. In this case, the constraints from direct detection data as well as the competing fermionic decays of the heavy Higgses stringently constrain the invisible decay  $H \rightarrow \chi\bar{\chi} \simeq 4.8\%$ . Owing to the small branching fraction and heavy mass of  $H$ , it is difficult to observe such a scenario due to the low production cross-section times branching ratio. We perform a signal-background analyses at the  $e^+e^-$  collider with  $\sqrt{s} = 3$  TeV with unpolarised beams and observe that the  $2b + \cancel{E}_T$  channel is observable with a  $= 3.99\sigma$  significance at integrated luminosity  $\mathcal{L} = 5 \text{ ab}^{-1}$ .

## Acknowledgements

JD and GMP acknowledge support by the Deutsche Forschungsgemeinschaft (DFG, German Research Foundation) under Germany's Excellence Strategy EXC 2121 "Quantum Universe"- 390833306. The authors thank G.Belanger, A.Pukhov from the micrOMEGAs team, J.Heisig, O.Mattalea and C.Arina from the maDDM team for helpful correspondence. The authors also thank H.Bahl, S.Heinemeyer, C.Li, S. Paasch, T.Stefaniak and G.Weiglein for helpful discussions and help with HiggsBounds and HiggsSignals.

## Appendix

### DM interaction vertices

We discuss the relevant interaction vertices of the DM and Higgses.

#### DM-scalar Higgs cubic interactions

$$\lambda_{hSS} = 2i \frac{v}{\sqrt{1 + \tan^2 \beta}} (\lambda'_4 \sin \alpha - \lambda'_5 \tan \beta \cos \alpha) \quad (9.1)$$

$$\lambda_{hSS^*} = i \frac{v}{\sqrt{1 + \tan^2 \beta}} (\lambda'_1 \sin \alpha - \lambda'_2 \tan \beta \cos \alpha) \quad (9.2)$$

$$\lambda_{hS^*S^*} = 2i \frac{v}{\sqrt{1 + \tan^2 \beta}} (\lambda'_4 \sin \alpha - \lambda'_5 \tan \beta \cos \alpha) \quad (9.3)$$

$$\lambda_{HSS} = -2i \frac{v}{\sqrt{1 + \tan^2 \beta}} (\lambda'_4 \cos \alpha + \lambda'_5 \tan \beta \sin \alpha) \quad (9.4)$$

$$\lambda_{HSS^*} = -i \frac{v}{\sqrt{1 + \tan^2 \beta}} (\lambda'_1 \cos \alpha + \lambda'_2 \tan \beta \sin \alpha) \quad (9.5)$$

$$\lambda_{HS^*S^*} = -2i \frac{v}{\sqrt{1 + \tan^2 \beta}} (\lambda'_4 \cos \alpha + \lambda'_5 \tan \beta \sin \alpha) \quad (9.6)$$

#### DM-Higgs scalars quartic interactions

$$\lambda_{hhSS} = -2i(\lambda'_4 \sin^2 \alpha + \lambda'_5 \cos^2 \alpha) \quad (9.7)$$

$$\lambda_{hhS^*S^*} = -2i(\lambda'_4 \sin^2 \alpha + \lambda'_5 \cos^2 \alpha) \quad (9.8)$$

$$\lambda_{hhSS^*} = -i(\lambda'_1 \sin^2 \alpha + \lambda'_2 \cos^2 \alpha) \quad (9.9)$$

$$\lambda_{hHSS} = i(\lambda'_4 - \lambda'_5) \sin 2\alpha \quad (9.10)$$

$$\lambda_{hHS^*S^*} = 2i(\lambda'_4 - \lambda'_5) \sin 2\alpha \quad (9.11)$$

$$\lambda_{HHSS} = -2i(\lambda'_4 \cos^2 \alpha + \lambda'_5 \sin^2 \alpha) \quad (9.12)$$

$$\lambda_{HHS^*S^*} = -2i(\lambda'_4 \cos^2 \alpha + \lambda'_5 \sin^2 \alpha) \quad (9.13)$$

### Pseudoscalar interactions with DM

$$\lambda_{AASS} = -2i\left(\frac{\lambda'_4 \tan^2 \beta}{1 + \tan^2 \beta} + \frac{\lambda'_5}{1 + \tan^2 \beta}\right) \quad (9.14)$$

$$\lambda_{AASS^*} = i\left(\frac{\lambda'_1 \tan^2 \beta}{1 + \tan^2 \beta} - \frac{\lambda'_2}{1 + \tan^2 \beta}\right) \quad (9.15)$$

$$\lambda_{AAS^*S^*} = -2i\left(\frac{\lambda'_4 \tan^2 \beta}{1 + \tan^2 \beta} + \frac{\lambda'_5}{1 + \tan^2 \beta}\right) \quad (9.16)$$

### Charged Higgs interactions with DM

$$\lambda_{H^+H^-SS} = -2i\left(\lambda'_4 \frac{\tan^2 \beta}{1 + \tan^2 \beta} + \lambda'_5 \frac{1}{1 + \tan^2 \beta}\right) \quad (9.17)$$

$$\lambda_{H^+H^-SS^*} = -i\left(\lambda'_1 \frac{\tan^2 \beta}{1 + \tan^2 \beta} + \lambda'_2 \frac{1}{1 + \tan^2 \beta}\right) \quad (9.18)$$

$$\lambda_{H^+H^-S^*S^*} = -2i\left(\lambda'_4 \frac{\tan^2 \beta}{1 + \tan^2 \beta} + \lambda'_5 \frac{1}{1 + \tan^2 \beta}\right) \quad (9.19)$$

### DM self interactions

$$\lambda_{SSSS} = -i\lambda''_1 \quad (9.20)$$

$$\lambda_{SSS^*S^*} = -i\lambda''_3 \quad (9.21)$$

$$\lambda_{SSSS^*} = -i\lambda''_1 \quad (9.22)$$

$$\lambda_{S^*S^*S^*S^*} = -i\lambda''_1 \quad (9.23)$$

$$\lambda_{S^*S^*S^*S^*} = -i\lambda''_1 \quad (9.24)$$

### Analytical computation of direct detection cross-section

We compute the direct detection cross-section. The DM-quark amplitude of the tree-level Feynman diagram Fig. 4 for zero momentum transfer is

$$\mathcal{M} = \sum_{h_i} \lambda_{h_i SS^*} \frac{1}{-m_{h_i}^2} \lambda_{h_i q\bar{q}} \quad (9.25)$$

where  $h_i = h, H$ . Recall,

$$\lambda_{hSS^*} = \frac{i}{\sqrt{1 + \tan^2 \beta}} (\lambda'_1 \sin \alpha - \lambda'_2 \tan \beta \cos \alpha)$$

$$\lambda_{HSS^*} = -\frac{i}{\sqrt{1 + \tan^2 \beta}} (\lambda'_1 \cos \alpha - \lambda'_2 \tan \beta \sin \alpha),$$

and

$$\lambda_{h_i q\bar{q}} = \frac{m_q}{v} C^{h_i}$$

is the Yukawa coupling of the quark to the Higgses. For Type II 2HDM[4] the Higgs couplings to the fermions are summarised in Table 14.

| Higgses | $C_u$                      | $C_d$                       | $C_s$                       |
|---------|----------------------------|-----------------------------|-----------------------------|
| $h$     | $\cos \alpha / \sin \beta$ | $-\sin \alpha / \cos \beta$ | $-\sin \alpha / \cos \beta$ |
| $H$     | $\sin \alpha / \sin \beta$ | $\cos \alpha / \cos \beta$  | $\cos \alpha / \cos \beta$  |

**Table 14.** The couplings of the fermions in Type II 2HDM[4].

In order to compute the DM-nucleon amplitude, the nucleon form factors  $f_N$  need to be folded into the quark-DM amplitude  $\mathcal{M}$ . The form factors  $f^N$  for  $N = p, n$  are[6]

$$f_N = \frac{m_N}{2m_\chi} \left( \sum_{q=u,d,s} f_{Tq}^N \frac{\mathcal{M}}{m_q} + \frac{2}{27} f_{TG}^N \sum_{q=c,b,t} \frac{\mathcal{M}}{m_q} \right) \quad (9.26)$$

where the first term is due to the contribution of the light valence quarks and the second term due to the gluonic form factor  $f_{TG}^N$  defined as,

$$f_{TG}^N = 1 - \sum_{q=u,d,s} f_{Tq}^N \quad (9.27)$$

Folding in the form factors above and the phase space of the DM-nucleon scattering, the DM-nucleon cross-section for the proton and neutron are[6, 63],

$$\sigma_{SI}^p = \frac{4\mu_N^2}{\pi} (Z f_p)^2 \quad (9.28)$$

$$\sigma_{SI}^n = \frac{4\mu_N^2}{\pi} ((A - Z) f_n)^2 \quad (9.29)$$

where  $\mu_N = \frac{m_\chi m_N}{(m_\chi + m_N)}$  for nucleon  $N = p, n$ .

## References

- [1] V. Barger, P. Langacker, M. McCaskey, M. Ramsey-Musolf, and G. Shaughnessy, *Complex Singlet Extension of the Standard Model*, *Phys. Rev. D* **79** (2009) 015018, [[arXiv:0811.0393](#)].
- [2] H. Wu and S. Zheng, *Scalar Dark Matter: Real vs Complex*, *JHEP* **03** (2017) 142, [[arXiv:1610.06292](#)].
- [3] **XENON** Collaboration, E. Aprile et al., *Dark Matter Search Results from a One Ton-Year Exposure of XENON1T*, *Phys. Rev. Lett.* **121** (2018), no. 11 111302, [[arXiv:1805.12562](#)].
- [4] G. Branco, P. Ferreira, L. Lavoura, M. Rebelo, M. Sher, and J. P. Silva, *Theory and phenomenology of two-Higgs-doublet models*, *Phys. Rept.* **516** (2012) 1–102, [[arXiv:1106.0034](#)].
- [5] G. C. Dorsch, S. J. Huber, T. Konstandin, and J. M. No, *A Second Higgs Doublet in the Early Universe: Baryogenesis and Gravitational Waves*, *JCAP* **05** (2017) 052, [[arXiv:1611.05874](#)].
- [6] A. Drozd, B. Grzadkowski, J. F. Gunion, and Y. Jiang, *Extending two-Higgs-doublet models by a singlet scalar field - the Case for Dark Matter*, *JHEP* **11** (2014) 105, [[arXiv:1408.2106](#)].
- [7] M. Muhlleitner, M. O. P. Sampaio, R. Santos, and J. Wittbrodt, *The N2HDM under Theoretical and Experimental Scrutiny*, *JHEP* [[arXiv:1612.01309](#)].
- [8] A. Dey, J. Lahiri, and B. Mukhopadhyaya, *LHC signals of a heavy doublet Higgs as dark matter portal: cut-based approach and improvement with gradient boosting and neural networks*, *JHEP* **09** (2019) 004, [[arXiv:1905.02242](#)].
- [9] S. Baum and N. R. Shah, *Two Higgs Doublets and a Complex Singlet: Disentangling the Decay Topologies and Associated Phenomenology*, [arXiv:1808.02667](#). [[JHEP12,044\(2018\)](#)].
- [10] T. Biekötter and M. O. Olea-Romacho, *Reconciling Higgs physics and pseudo-Nambu-Goldstone dark matter in the S2HDM using a genetic algorithm*, *JHEP* **10** (2021) 215, [[arXiv:2108.10864](#)].
- [11] K. Kannike, K. Loos, and M. Raidal, *Gravitational wave signals of pseudo-Goldstone dark matter in the  $\mathbb{Z}_3$  complex singlet model*, *Phys. Rev. D* **101** (2020), no. 3 035001, [[arXiv:1907.13136](#)].
- [12] D. G. E. Walker, *Dark Matter Stabilization Symmetries from Spontaneous Symmetry Breaking*, [arXiv:0907.3146](#).
- [13] B. Batell, *Dark Discrete Gauge Symmetries*, *Phys. Rev. D* **83** (2011) 035006, [[arXiv:1007.0045](#)].
- [14] C. Gross, O. Lebedev, and T. Toma, *Cancellation Mechanism for*

- Dark-Matter–Nucleon Interaction*, *Phys. Rev. Lett.* **119** (2017), no. 19 191801, [[arXiv:1708.02253](#)].
- [15] C. Cai, Y.-P. Zeng, and H.-H. Zhang, *Cancellation mechanism of dark matter direct detection in Higgs-portal and vector-portal models*, [arXiv:2109.11499](#).
- [16] **Fermi-LAT Collaboration**, M. Ackermann et al., *Constraining Dark Matter Models from a Combined Analysis of Milky Way Satellites with the Fermi Large Area Telescope*, *Phys. Rev. Lett.* **107** (2011) 241302, [[arXiv:1108.3546](#)].
- [17] **ATLAS Collaboration** Collaboration, *Measurement of the Higgs boson mass in the  $H \rightarrow ZZ^* \rightarrow 4\ell$  decay channel with  $\sqrt{s} = 13$  TeV pp collisions using the ATLAS detector at the LHC*, Tech. Rep. ATLAS-CONF-2020-005, CERN, Geneva, Apr, 2020.
- [18] **ATLAS Collaboration**, *Combination of searches for invisible Higgs boson decays with the ATLAS experiment*, .
- [19] **CMS Collaboration**, A. M. Sirunyan et al., *Search for invisible decays of a Higgs boson produced through vector boson fusion in proton-proton collisions at  $\sqrt{s} = 13$  TeV*, *Phys. Lett. B* **793** (2019) 520–551, [[arXiv:1809.05937](#)].
- [20] **BaBar Collaboration** Collaboration, J. Lees et al., *Precision Measurement of the  $B \rightarrow X_s \gamma$  Photon Energy Spectrum, Branching Fraction, and Direct CP Asymmetry  $A_{CP}(B \rightarrow X_{s+d} \gamma)$* , *Phys.Rev.Lett.* **109** (2012) 191801, [[arXiv:1207.2690](#)].
- [21] **LHCb collaboration** Collaboration, R. Aaij et al., *Measurement of the  $B_s^0 \rightarrow \mu^+ \mu^-$  branching fraction and search for  $B^0 \rightarrow \mu^+ \mu^-$  decays at the LHCb experiment*, *Phys.Rev.Lett.* **111** (2013) 101805, [[arXiv:1307.5024](#)].
- [22] **CMS Collaboration** Collaboration, S. Chatrchyan et al., *Measurement of the  $B(s)$  to  $mu+$   $mu-$  branching fraction and search for  $B0$  to  $mu+$   $mu-$  with the CMS Experiment*, *Phys.Rev.Lett.* **111** (2013) 101804, [[arXiv:1307.5025](#)].
- [23] <https://pdg.lbl.gov/2020/reviews/rpp2020-rev-g-2-muon-anom-mag-moment.pdf>.
- [24] P. D. Group and P. A. e. Zyla, *Review of Particle Physics*, *Progress of Theoretical and Experimental Physics* **2020** (08, 2020) [<https://academic.oup.com/ptep/article-pdf/2020/8/083C01/33653179/ptaa104.pdf>]. 083C01.
- [25] **Planck Collaboration**, N. Aghanim et al., *Planck 2018 results. VI. Cosmological parameters*, *Astron. Astrophys.* **641** (2020) A6, [[arXiv:1807.06209](#)].
- [26] **ALEPH, DELPHI, L3, OPAL, LEP Collaboration**, G. Abbiendi et al., *Search for Charged Higgs bosons: Combined Results Using LEP Data*, *Eur. Phys. J. C* **73** (2013) 2463, [[arXiv:1301.6065](#)].
- [27] **ATLAS Collaboration**. <https://atlas.web.cern.ch/Atlas/GROUPS/PHYSICS/CombinedSummaryPlots/HDBS/>.

- [28] CMS Collaboration, <https://twiki.cern.ch/twiki/bin/view/CMSPublic/Summary2HDMSRun2>.
- [29] **ATLAS Collaboration** Collaboration, *A combination of measurements of Higgs boson production and decay using up to  $139 \text{ fb}^{-1}$  of proton–proton collision data at  $\sqrt{s} = 13 \text{ TeV}$  collected with the ATLAS experiment*, Tech. Rep. ATLAS-CONF-2020-027, CERN, Geneva, Aug, 2020.
- [30] O. Eberhardt, *Current status of Two-Higgs-Doublet models with a softly broken  $\mathbb{Z}_2$  symmetry*, *PoS ICHEP2018* (2019) 457, [[arXiv:1809.04851](#)].
- [31] A. Arbey, F. Mahmoudi, O. Stal, and T. Stefaniak, *Status of the Charged Higgs Boson in Two Higgs Doublet Models*, *Eur. Phys. J. C* **78** (2018), no. 3 182, [[arXiv:1706.07414](#)].
- [32] G. Belanger, F. Boudjema, A. Pukhov, A. Semenov, and et al., *The user’s manual, version 5.2*, [http://lapth.cnrs.fr/micromegas/v5.2/manual\\_5.2.pdf](http://lapth.cnrs.fr/micromegas/v5.2/manual_5.2.pdf), .
- [33] P. Bechtle, S. Heinemeyer, T. Klingl, T. Stefaniak, G. Weiglein, and J. Wittbrodt, *HiggsSignals-2: Probing new physics with precision Higgs measurements in the LHC 13 TeV era*, *Eur. Phys. J. C* **81** (2021), no. 2 145, [[arXiv:2012.09197](#)].
- [34] W. Porod, *SPheno, a program for calculating supersymmetric spectra, SUSY particle decays and SUSY particle production at  $e^+ e^-$  colliders*, *Comput. Phys. Commun.* **153** (2003) 275–315, [[hep-ph/0301101](#)].
- [35] F. Staub, *SARAH 4 : A tool for (not only SUSY) model builders*, *Comput. Phys. Commun.* **185** (2014) 1773–1790, [[arXiv:1309.7223](#)].
- [36] G. Arcadi, G. Busoni, T. Hugle, and V. T. Tenorth, *Comparing 2HDM + Scalar and Pseudoscalar Simplified Models at LHC*, *JHEP* **06** (2020) 098, [[arXiv:2001.10540](#)].
- [37] P. Bechtle, D. Dercks, S. Heinemeyer, T. Klingl, T. Stefaniak, G. Weiglein, and J. Wittbrodt, *HiggsBounds-5: Testing Higgs Sectors in the LHC 13 TeV Era*, [arXiv:2006.06007](#).
- [38] P. Bechtle, S. Heinemeyer, O. Stal, T. Stefaniak, and G. Weiglein, *HiggsSignals: Confronting arbitrary Higgs sectors with measurements at the Tevatron and the LHC*, *Eur. Phys. J. C* **74** (2014), no. 2 2711, [[arXiv:1305.1933](#)].
- [39] J. Alwall, M. Herquet, F. Maltoni, O. Mattelaer, and T. Stelzer, *MadGraph 5 : Going Beyond*, *JHEP* **06** (2011) 128, [[arXiv:1106.0522](#)].
- [40] J. Alwall, R. Frederix, S. Frixione, V. Hirschi, F. Maltoni, O. Mattelaer, H. S. Shao, T. Stelzer, P. Torrielli, and M. Zaro, *The automated computation of tree-level and next-to-leading order differential cross sections, and their matching to parton shower simulations*, *JHEP* **07** (2014) 079, [[arXiv:1405.0301](#)].
- [41] Pythia. <http://home.thep.lu.se/~torbjorn/pythia81html/Welcome.html>.
- [42] **DELPHES 3** Collaboration, J. de Favereau, C. Delaere, P. Demin, A. Giammanco, V. Lemaître, A. Mertens, and M. Selvaggi, *DELPHES 3, A modular framework for*

- fast simulation of a generic collider experiment*, *JHEP* **02** (2014) 057, [[arXiv:1307.6346](#)].
- [43] M. Selvaggi, *DELPHES 3: A modular framework for fast-simulation of generic collider experiments*, *J. Phys. Conf. Ser.* **523** (2014) 012033.
- [44] A. Mertens, *New features in Delphes 3*, *J. Phys. Conf. Ser.* **608** (2015), no. 1 012045.
- [45] B. Dumont, B. Fuks, S. Kraml, S. Bein, G. Chalons, E. Conte, S. Kulkarni, D. Sengupta, and C. Wymant, *Toward a public analysis database for LHC new physics searches using MADANALYSIS 5*, *Eur. Phys. J. C* **75** (2015), no. 2 56, [[arXiv:1407.3278](#)].
- [46] E. Conte, B. Dumont, B. Fuks, and C. Wymant, *Designing and recasting LHC analyses with MadAnalysis 5*, *Eur. Phys. J. C* **74** (2014), no. 10 3103, [[arXiv:1405.3982](#)].
- [47] E. Conte and B. Fuks, *Confronting new physics theories to LHC data with MADANALYSIS 5*, *Int. J. Mod. Phys. A* **33** (2018), no. 28 1830027, [[arXiv:1808.00480](#)].
- [48] J. Y. Araz, M. Frank, and B. Fuks, *Reinterpreting the results of the LHC with MadAnalysis 5: uncertainties and higher-luminosity estimates*, *Eur. Phys. J. C* **80** (2020), no. 6 531, [[arXiv:1910.11418](#)].
- [49] J. Y. Araz, B. Fuks, and G. Polykratis, *Simplified fast detector simulation in MADANALYSIS 5*, *Eur. Phys. J. C* **81** (2021), no. 4 329, [[arXiv:2006.09387](#)].
- [50] **ATLAS, CMS Collaboration**, *Addendum to the report on the physics at the HL-LHC, and perspectives for the HE-LHC: Collection of notes from ATLAS and CMS*, *CERN Yellow Rep. Monogr.* **7** (2019) Addendum, [[arXiv:1902.10229](#)].
- [51] A. Adhikary, S. Banerjee, R. Kumar Barman, and B. Bhattacharjee, *Resonant heavy Higgs searches at the HL-LHC*, *JHEP* **09** (2019) 068, [[arXiv:1812.05640](#)].
- [52] H. Bahl, P. Bechtle, S. Heinemeyer, S. Liebler, T. Stefaniak, and G. Weiglein, *HL-LHC and ILC sensitivities in the hunt for heavy Higgs bosons*, *Eur. Phys. J. C* **80** (2020), no. 10 916, [[arXiv:2005.14536](#)].
- [53] **ATLAS Collaboration**, G. Aad et al., *Search for new phenomena in events with an energetic jet and missing transverse momentum in  $pp$  collisions at  $\sqrt{s} = 13$  TeV with the ATLAS detector*, *Phys. Rev. D* **103** (2021), no. 11 112006, [[arXiv:2102.10874](#)].
- [54] **ATLAS Collaboration** Collaboration, *Search for invisible Higgs boson decays with vector boson fusion signatures with the ATLAS detector using an integrated luminosity of  $139 \text{ fb}^{-1}$* , tech. rep., CERN, Geneva, Apr, 2020. All figures including auxiliary figures are available at <https://atlas.web.cern.ch/Atlas/GROUPS/PHYSICS/CONFNOTES/ATLAS-CONF-2020-008>.
- [55] T. Behnke, J. E. Brau, B. Foster, J. Fuster, M. Harrison, J. M. Paterson, M. Peskin, M. Stanitzki, N. Walker, and H. Yamamoto, *The International Linear Collider*

*Technical Design Report - Volume 1: Executive Summary*, [arXiv:1306.6327](https://arxiv.org/abs/1306.6327). See also <http://www.linearcollider.org/ILC/TDR>. The full list of contributing institutes is inside the Report.

- [56] G. Moortgat-Pick et al., *The Role of polarized positrons and electrons in revealing fundamental interactions at the linear collider*, *Phys. Rept.* **460** (2008) 131–243, [[hep-ph/0507011](https://arxiv.org/abs/hep-ph/0507011)].
- [57] **CLICdp, CLIC Collaboration**, T. K. Charles et al., *The Compact Linear Collider (CLIC) - 2018 Summary Report*, [arXiv:1812.06018](https://arxiv.org/abs/1812.06018).
- [58] P. G. Roloff and A. Robson, *Updated CLIC luminosity staging baseline and Higgs coupling prospects*, tech. rep., CERN, Geneva, Oct, 2018. 9 pages, 6 figures.
- [59] A. Blondel, J. Gluza, S. Jadach, P. Janot, and T. Riemann, eds., *Theory for the FCC-ee: Report on the 11th FCC-ee Workshop Theory and Experiments*, vol. 3/2020 of *CERN Yellow Reports: Monographs*, (Geneva), CERN, 5, 2019.
- [60] **CEPC Study Group** Collaboration, M. Dong et al., *CEPC Conceptual Design Report: Volume 2 - Physics & Detector*, [arXiv:1811.10545](https://arxiv.org/abs/1811.10545).
- [61] G. Cowan, K. Cranmer, E. Gross, and O. Vitells, *Asymptotic formulae for likelihood-based tests of new physics*, *Eur. Phys. J. C* **71** (2011) 1554, [[arXiv:1007.1727](https://arxiv.org/abs/1007.1727)]. [Erratum: *Eur.Phys.J.C* 73, 2501 (2013)].
- [62] <https://pdg.lbl.gov/2019/reviews/rpp2018-rev-statistics.pdf>, .
- [63] G. Jungman, M. Kamionkowski, and K. Griest, *Supersymmetric dark matter*, *Phys. Rept.* **267** (1996) 195–373, [[hep-ph/9506380](https://arxiv.org/abs/hep-ph/9506380)].